A new time-domain finite element method for simulating surface plasmon polaritons on graphene sheets

Jichun Li * Li Zhu † Todd Arbogast ‡

May 6, 2023

Abstract

In this paper, we develop a new variational form to simulate the propagation of surface plasmon polaritons on graphene sheets. Here the graphene is treated as a thin sheet of current with an effective conductivity, and modeled as a lower-dimensional interface. A novel time-domain finite element method is proposed for solving this graphene model, which coupled an ordinary differential equation on the interface with Maxwell's equations in the physical domain. Discrete stability and error estimate are proved for our proposed method. Numerical results are presented to demonstrate the effectiveness of this graphene model for simulating the surface plasmon polaritons propagating on graphene sheets.

Keywords – Maxwell's equations, finite element time-domain methods, edge elements, graphene.
Mathematics Subject Classification (2000): 78M10, 65N30, 65F10, 78-08.

1 Introduction

The two-dimensional (2-D) material graphene was rediscovered, isolated and investigated by Novoselov, Geim and co-workers [30] in 2004. The 2010 Nobel Prize in Physics was awarded to Geim and Novoselov "for groundbreaking experiments regarding the two-dimensional material graphene." Since 2004, graphene has become a valuable and useful nanomaterial, and its study has become a very hot research topic [4,12,35] due to its exceptionally high tensile strength, high electronic mobility, high thermal conductivity, low absorption of light, and being the thinnest two-dimensional material in the world.

Numerical simulation of electromagnetic wave propagation plays a very important role in the study of graphene and its applications. The finite difference time-domain (FDTD) method

*Department of Mathematical Sciences, University of Nevada Las Vegas, Nevada 89154-4020, USA (jichun.li@unlv.edu)

†Department of Mathematical Sciences, University of Nevada Las Vegas, Nevada 89154-4020, USA (zhul5@unlv.nevada.edu).

‡Department of Mathematics, University of Texas at Austin, Austin, Texas 78712-1202, USA (arbogast@oden.utexas.edu)

(e.g., [1,11,14,15,19,24,40]) and the finite element method (FEM) (e.g., [3,6–8,10,16,17,21,31]) are arguably the two most popular numerical methods in computational electromagnetics, which can solve Maxwell's equations in various media. More details and references on the FDTD method and FEM for Maxwell's equations can be found in related FDTD books [34] and FEM books [9, 22, 28].

Compared to many existing papers on simulation of graphene and its applications by FDTD methods [5, 27, 29], there are quite limited publications on FEMs for graphene simulation, e.g., [23, 37] are on discontinuous Galerkin time-domain (DGTD) modeling of graphene devices, and [26, 33] are on frequency-domain finite element simulation of graphene sheet. Recently, Li and collaborators [18, 20, 39] have proposed and analyzed some finite element time-domain (FETD) methods for graphene simulation. In [18, 20, 39], the graphene has been treated with some thickness (though very thin). A major drawback of this approach is that a particularly fine spatial mesh is needed for the graphene part, which makes the implementation time consuming. Mathematical analysis of graphene model in time domain is very limited. In a recent work [38], the authors investigated the effects of modulating the electronic doping of graphene in time on plasmon dynamics, and they also established the existence, uniqueness, and regularity for solutions to the resulting current equation. In this paper, we will investigate a time-domain graphene model and treat the graphene as an infinitesimal thin conductive sheet. For the first time a new finite element time-domain method is proposed and analyzed for solving this graphene model.

The rest of the paper is organized as follows. In Section 2, we first present the time-domain governing equations for modeling the surface plasmon polaritons on the graphene sheet. Then we prove an energy identity and a stability for the system of the modeling equations. In Section 3, we propose a leapfrog type scheme for solving the modeling equations, and prove the discrete stability and the optimal error estimate for our scheme. In Section 4, we present extensive numerical results to demonstrate the propagation of surface plasmon polaritons appearing on various graphene sheets. We conclude the paper in Section 5.

2 The governing equations and stability analysis

We assume that Ω is a bounded Lipschitz polygonal domain in $\mathcal{R}^2$ with boundary $\partial\Omega$. In our previous works [18,20,39], we treated the graphene as a homogenized material of small thickness with an effective permittivity. Here we adopt another way to treat graphene as a thin sheet of current with an effective conductivity.

Considering that the interband conductivity is not that significant in most cases, we will ignore it in this paper. For simplicity, we consider the TE_z mode problem with electric field $\boldsymbol{E} = (E_x, E_y)'$ and magnetic field $H = H_z$. From [39, (2.7)-(2.12)] (see also [18, (2.10)-(2.13)]), we have the following governing equations for simulating surface plasmon propagation on graphene:

$$\epsilon_0 \partial_t \boldsymbol{E} = \nabla \times H, \quad \text{in } \Omega, \tag{2.1}$$

$$\mu_0 \partial_t H = -\nabla \times \boldsymbol{E} - K_s, \quad \text{in } \Omega, \tag{2.2}$$

$$\tau_0 \partial_t \boldsymbol{J} + \boldsymbol{J} = \sigma_0 \boldsymbol{E}, \quad \text{on } \Gamma, \tag{2.3}$$

where K_s is an imposed magnetic source function, $\boldsymbol{J} := \boldsymbol{J}_d$ (as denoted in [39]) is the induced intraband surface current in graphene, ϵ_0 and μ_0 are respectively the permittivity and permeability in vacuum, the positive constant τ_0 denotes the relaxation time, and the positive constant σ_0 denotes the graphene surface conductivity. Here Γ represents the graphene sheet buried in the domain Ω. It appears as a line in our 2D domain (cf. Figures 1, 3, 5, and 7 shown later). Finally, the 2D curl operators are defined as $\nabla \times H := (\partial_y H, -\partial_x H)'$ and $\nabla \times \boldsymbol{E} := \partial_x E_y - \partial_y E_x$.

According to [2, Fig.1], the boundary conditions on the graphene interface are:

$$\hat{n}_1 \times \boldsymbol{E}_1 = \hat{n}_2 \times \boldsymbol{E}_2, \quad \text{on } \Gamma, \tag{2.4}$$

$$H_1 - H_2 = \boldsymbol{J} \times \hat{n}, \quad \text{on } \Gamma, \tag{2.5}$$

which mean that the tangential electric field is continuous across the interface, and the jump of the tangential component of the magnetic field along the interface is equal to the surface current. Here H_1 and H_2 represent the magnetic field above and below the interface, respective, $\hat{n} := (n_x, n_y)'$ is the unit normal vector pointing upward, and $\hat{n}_1$ and $\hat{n}_2$ are the unit outward normal vectors from top and bottom subdomains of the interface. Here we denote the 2D cross product $\boldsymbol{J} \times \hat{n} := J_x n_y - J_y n_x$.

We remark that (2.3) was originally developed for a graphene sheet with small thickness in [39]. For an infinitely thin graphene sheet, the surface current must lie within Γ, and so the equation must be interpreted as

$$\tau_0 \partial_t (\boldsymbol{J} \times \hat{n}) + \boldsymbol{J} \times \hat{n} = \sigma_0 \boldsymbol{E} \times \hat{n}. \tag{2.6}$$

To complete the problem, we assume that (2.1)-(2.3) is subject to the perfectly conducting (PEC) boundary condition:

$$\hat{\nu} \times \boldsymbol{E} = 0, \quad \text{on } \partial\Omega, \tag{2.7}$$

and the initial conditions

$$\boldsymbol{E}(\boldsymbol{x}, 0) = \boldsymbol{E}_0(\boldsymbol{x}), \ H(\boldsymbol{x}, 0) = H_0(\boldsymbol{x}), \ \boldsymbol{J}(\boldsymbol{x}, 0)|_\Gamma = \boldsymbol{J}_0(\boldsymbol{x})|_\Gamma, \tag{2.8}$$

where $\hat{\nu}$ is the unit outward normal vector on $\partial\Omega$, and $\boldsymbol{E}_0, H_0, \boldsymbol{J}_0$ are some given functions.

We want to remark that the system (2.1)-(2.8) can be used to model the propagation of the surface plasmon polaritons on graphene, which is usually embedded inside other materials such as vacuum. Moreover, the system (2.1)-(2.3) can be reduced to the standard Maxwell's equations in vacuum by setting $\boldsymbol{J}$ to be zero and ignoring (2.3).

Denote the Sobolev space

$$H_0(\text{curl}; \Omega) = \{\boldsymbol{u} \in (L^2(\Omega))^2 : \ \nabla \times \boldsymbol{u} \in L^2(\Omega), \ \hat{\nu} \times \boldsymbol{u} = 0 \text{ on } \partial\Omega\}.$$

We can easily obtain the following weak formulation: Find the solution

$$\boldsymbol{E} \in L^2(0, T; H_0(\text{curl}; \Omega)) \cap H^1(0, T; (L^2(\Omega))^2), H \in H^1(0, T; L^2(\Omega)), \boldsymbol{J} \in H^1(0, T; (L^2(\Gamma))^2),$$

such that

$$\epsilon_0 (\partial_t \boldsymbol{E}, \boldsymbol{\phi}) = (H, \nabla \times \boldsymbol{\phi}) - \langle \boldsymbol{J}, \boldsymbol{\phi} \rangle_\Gamma \tag{2.9}$$

$$\mu_0(\partial_t H, \psi) = -(\nabla \times \boldsymbol{E}, \psi) - (K_s, \psi) \tag{2.10}$$

$$\langle \tau_0 \partial_t \boldsymbol{J}, \boldsymbol{\chi} \rangle_\Gamma + \langle \boldsymbol{J}, \boldsymbol{\chi} \rangle_\Gamma = \langle \sigma_0 \boldsymbol{E}, \boldsymbol{\chi} \rangle_\Gamma \tag{2.11}$$

hold true for any test functions $\boldsymbol{\phi} \in H_0(curl; \Omega), \psi \in L^2(\Omega)$ and $\boldsymbol{\chi} \in (L^2(\Gamma))^2$. To obtain (2.9), we use the integration by parts over Ω and the boundary condition (2.5). Here and below we denote $(\cdot, \cdot)$ for the inner product over Ω, and $\langle \boldsymbol{J}, \boldsymbol{\phi} \rangle_\Gamma := \int_\Gamma \boldsymbol{J} \times \hat{n} \cdot \boldsymbol{\phi} \times \hat{n}\, ds$ for the inner product on Γ. Only $\boldsymbol{J} \times \hat{n}$ is determined by the differential and variational formulations, and only the component $\boldsymbol{\chi} \times \hat{n}$ of $\boldsymbol{\chi}$ is used as a test function.

To simplify the notation, we denote the L^2 norm of u in Ω as $||u|| := ||u||_{L^2(\Omega)}$, and the L^2 norm of $\boldsymbol{u}$ on Γ as $||\boldsymbol{u}||_\Gamma := (\int_\Gamma |\boldsymbol{u} \times \hat{n}|^2\, ds)^{1/2}$.

Theorem 2.1. *For the solution $(\boldsymbol{E}, H, \boldsymbol{J})$ of (2.9)-(2.11), the following energy identity holds true for any $t \in [0, T]$:*

$$ENG(t) - ENG(0) + \int_0^t \frac{2}{\sigma_0} \|\boldsymbol{J}\|_\Gamma^2 dt = -\int_0^t 2(K_s, H) dt, \tag{2.12}$$

where we denote the energy

$$ENG(t) \quad := \quad \left[\epsilon_0 \|\boldsymbol{E}\|^2 + \mu_0 \|H\|^2 + \frac{\tau_0}{\sigma_0} \|\boldsymbol{J}\|_\Gamma^2 \right](t). \tag{2.13}$$

Furthermore, we have the following continuous stability:

$$ENG(t) \le \left[ENG(0) + \int_0^t \frac{1}{\mu_0} \|K_s\|^2 dt \right] \cdot \exp(t), \quad \forall\ t \in [0, T]. \tag{2.14}$$

Proof. By choosing $\boldsymbol{\phi} = 2\boldsymbol{E}, \psi = 2H, \boldsymbol{\chi} = \frac{2}{\sigma_0}\boldsymbol{J}$ in (2.9)-(2.11), respectively, then adding the results together, we have

$$\frac{d}{dt} \left(\epsilon_0 \|\boldsymbol{E}\|^2 + \mu_0 \|H\|^2 + \frac{\tau_0}{\sigma_0} \|\boldsymbol{J}\|_\Gamma^2 \right) + \frac{2}{\sigma_0} \|\boldsymbol{J}\|_\Gamma^2 = -2(K_s, H). \tag{2.15}$$

Integrating (2.15) with respect to t from 0 to t, and using the energy notation defined by (2.13), we immediately have the energy identity (2.12).

Using the following Young's inequality

$$-\int_0^t 2(K_s, H) dt \le \int_0^t (\mu_0 \|H\|^2 + \frac{1}{\mu_o} \|K_s\|^2) dt,$$

in (2.12), and dropping the nonnegative term $\int_0^t \frac{\tau_0}{\sigma_0} \|\boldsymbol{J}\|_\Gamma^2 dt$ on the left hand side, we obtain

$$\begin{aligned} ENG(t) \quad &\le \quad \left[ENG(0) + \int_0^t \frac{1}{\mu_o} \|K_s\|^2 dt \right] + \int_0^t \mu_0 \|H\|^2 dt \\ &\le \quad \left[ENG(0) + \int_0^t \frac{1}{\mu_o} \|K_s\|^2 dt \right] + \int_0^t ENG(s) ds. \end{aligned} \tag{2.16}$$

The proof of (2.14) is completed by the Gronwall inequality applied to (2.16). ∎

3 The leapfrog finite element scheme and its analysis

To design a finite element method, we partition the physical domain Ω with Γ as an internal boundary by a shape regular triangular mesh $\mathcal{T}_h$ with maximum mesh size h. Without loss of generality, we consider the following Raviart-Thomas-Nédélec (RTN)'s mixed spaces U_h and $\boldsymbol{V}_h$ on triangular elements [22,28]: For any $r \geq 1$,

$$U_h = \{u_h \in L^2(\Omega) : \ u_h|_K \in p_{r-1}, \forall K \in T_h\},$$
$$\boldsymbol{V}_h = \{\boldsymbol{v}_h \in H(curl;\Omega) : \ \boldsymbol{v}_h|_K \in (p_{r-1})^2 \oplus S_r, \forall K \in T_h\}, \quad S_r = \{\overrightarrow{p} \in \tilde{p_r}^2, \boldsymbol{x} \cdot \overrightarrow{p} = 0\}.$$

To handle the PEC boundary condition (2.7), we introduce the subspace

$$\boldsymbol{V}_h^0 = \{\boldsymbol{v}_h \in \boldsymbol{V}_h : \quad \hat{\nu} \times \boldsymbol{v}_h = 0 \quad \text{on } \partial\Omega\}.$$

To construct the fully discrete finite element scheme, we partition the time interval $[0,T]$ uniformly by points $t_i = i\tau, i = 0, ..., N_t$, where $\tau = \frac{T}{N_t}$ denotes the time step size.

Now we can construct the following leapfrog type scheme: Given proper initial approximations of $\boldsymbol{E}_h^0 \in \boldsymbol{V}_h^0, \boldsymbol{J}_h^{\frac{1}{2}} \in \boldsymbol{W}_h$, $H_h^{\frac{1}{2}} \in U_h$, for any $n \geq 0$, find $\boldsymbol{E}_h^{n+1} \in \boldsymbol{V}_h^0$, $\boldsymbol{J}_h^{n+\frac{3}{2}} \in \boldsymbol{W}_h$ (i.e., $\boldsymbol{J}_h^{n+\frac{3}{2}} \times \hat{n} \in \boldsymbol{W}_h \times \hat{n}$), $H_h^{n+\frac{3}{2}} \in U_h$ such that

$$\epsilon_0(\delta_\tau \boldsymbol{E}_h^{n+\frac{1}{2}}, \boldsymbol{\phi}_h) = (H_h^{n+\frac{1}{2}}, \nabla \times \boldsymbol{\phi}_h) - \langle \boldsymbol{J}_h^{n+\frac{1}{2}}, \boldsymbol{\phi}_h \rangle_\Gamma, \tag{3.1}$$
$$\mu_0(\delta_\tau H_h^{n+1}, \psi_h) = -(\nabla \times \boldsymbol{E}_h^{n+1}, \psi_h) - (K_s^{n+1}, \psi_h), \tag{3.2}$$
$$\tau_0 \langle \delta_\tau \boldsymbol{J}_h^{n+1}, \boldsymbol{\chi}_h \rangle_\Gamma + \langle \overline{\boldsymbol{J}}_h^{n+1}, \boldsymbol{\chi}_h \rangle_\Gamma = \sigma_0 \langle \boldsymbol{E}_h^{n+1}, \boldsymbol{\chi}_h \rangle_\Gamma, \tag{3.3}$$

hold true for any test functions $\boldsymbol{\phi}_h \in \boldsymbol{V}_h^0, \psi_h \in U_h$ and $\boldsymbol{\chi}_h \in \boldsymbol{W}_h$. Here we choose

$$\boldsymbol{W}_h = \{\boldsymbol{w}_h \in (L^2(\Omega))^2 : \ \exists \ \boldsymbol{v}_h \in \boldsymbol{V}_h \text{ such that } \boldsymbol{v}_h \times \hat{n} = \boldsymbol{w}_h \text{ on } \Gamma\},$$

and adopt the following central difference operator and averaging operator in time: For any time sequence function u^n,

$$\delta_\tau u^{n+\frac{1}{2}} = \frac{u^{n+1} - u^n}{\tau}, \quad \overline{u}^{n+\frac{1}{2}} = \frac{u^{n+1} + u^n}{2}.$$

Corresponding to the finite element spaces $\boldsymbol{V}_h$ and U_h, we denote Π_c and Π_2 for the standard Nédélec interpolation in space $\boldsymbol{V}_h$ and the standard L^2 projection onto space U_h, respectively. Furthermore, the following interpolation and projection errors hold true (cf. [22,28]):

$$||\boldsymbol{u} - \Pi_c \boldsymbol{u}||_{H(\text{curl};\Omega)} \leq ch^r ||\boldsymbol{u}||_{H^r(\text{curl};\Omega)}, \quad \forall \ \boldsymbol{u} \in H^r(\text{curl};\Omega), \quad r \geq 1, \tag{3.4}$$
$$||u - \Pi_2 u||_{L^2(\Omega)} \leq ch^r ||u||_{H^r(\Omega)}, \quad \forall \ u \in H^r(\Omega), \quad r \geq 0, \tag{3.5}$$

where $||u||_{H^r(\Omega)}$ denotes the norm for the Sobolev space $H^r(\Omega)$, and $||\boldsymbol{u}||_{H^r(\text{curl};\Omega)} := (||\boldsymbol{u}||^2_{(H^r(\Omega))^2} + ||\nabla \times \boldsymbol{u}||^2_{H^r(\Omega)})^{1/2}$ is the norm for the Sobolev space

$$H^r(\text{curl};\Omega) = \{\boldsymbol{u} \in (H^r(\Omega))^2 : \ \nabla \times \boldsymbol{u} \in H^r(\Omega)\}.$$

The initial conditions (2.8) are discretized as follows:

$$\boldsymbol{E}_h^0 = \Pi_c \boldsymbol{E}_0(\boldsymbol{x}), \tag{3.6}$$

$$H_h^{\frac{1}{2}} = \Pi_2(H(\cdot,0) + \frac{\tau}{2}\partial_t H(\cdot,0)) = \Pi_2\left[H_0(\boldsymbol{x}) - \frac{\tau}{2\mu_0}(\nabla\times\boldsymbol{E}_0(\boldsymbol{x}) + K_s(\boldsymbol{x},0))\right], \tag{3.7}$$

$$\boldsymbol{J}_h^{\frac{1}{2}}\times\hat{n} = \Pi_2\left[(\boldsymbol{J}(\cdot,0) + \frac{\tau}{2}\partial_t\boldsymbol{J}(\cdot,0))\times\hat{n}\right] = \Pi_2\left[\boldsymbol{J}_0\times\hat{n} + \frac{\tau}{2\tau_0}(\sigma_0\boldsymbol{E}_0 - \boldsymbol{J}_0)\times\hat{n}\right], \tag{3.8}$$

where we use the Taylor expansion and the governing equations (2.2) and (2.3).

Below we will present the stability and convergence analysis for our scheme.

3.1 Stability analysis

To prove the discrete stability for the fully-discrete scheme, we denote the wave propagation speed in vacuum $C_v = \frac{1}{\sqrt{\epsilon_0\mu_0}} \approx 3\times10^8 m/s$, and introduce the standard inverse estimate:

$$||\nabla\times\phi_h|| \le C_{in}h^{-1}||\phi_h||, \quad \forall\ \phi_h \in \boldsymbol{V}_h, \tag{3.9}$$

and the trace estimate:

$$||\phi_h||_{L^2(\Gamma)} \le C_{tr}h^{-1/2}||\phi_h||_{L^2(\Omega)}, \quad \forall\ \phi_h \in \boldsymbol{V}_h, \tag{3.10}$$

where the positive constants C_{in} and C_{tr} are independent of the mesh size h.

Theorem 3.1. *Denote the discrete energy:*

$$ENG_{dis}(m) \quad := \quad \epsilon_0||\boldsymbol{E}_h^m||^2 + \mu_0||H_h^{m+\frac{1}{2}}||^2 + \frac{\tau_0}{\sigma_0}||\boldsymbol{J}_h^{m+\frac{1}{2}}||_\Gamma^2. \tag{3.11}$$

Then under the time step constraint:

$$\tau \le \min\left(\frac{1}{2}, \frac{h}{2C_vC_{in}}, \frac{h^{\frac{1}{2}}}{2C_{tr}}\sqrt{\frac{\epsilon_0\tau_0}{\sigma_0}}\right), \tag{3.12}$$

we have: For any $m \in [1, N_t-1]$,

$$ENG_{dis}(m) \le 2\left[ENG_{dis}(0) + \tau\sum_{n=0}^{m-1}\frac{1}{\mu_0}||K_s^{n+1}||^2\right]\exp(2m\tau). \tag{3.13}$$

Proof. Choosing $\boldsymbol{\phi}_h = 2\tau\overline{\boldsymbol{E}}_h^{n+\frac{1}{2}}$, $\psi_h = 2\tau\overline{H}_h^{n+1}$, $\boldsymbol{\chi}_h = \frac{2\tau}{\sigma_0}\overline{\boldsymbol{J}}_h^{n+1}$ in (3.1)-(3.3), respectively, then adding them together, we have

$$\begin{aligned}
&\epsilon_0(||\boldsymbol{E}_h^{n+1}||^2 - ||\boldsymbol{E}_h^n||^2) + \mu_0(||H_h^{n+\frac{3}{2}}||^2 - ||H_h^{n+\frac{1}{2}}||^2) + \frac{\tau_0}{\sigma_0}(||\boldsymbol{J}_h^{n+\frac{3}{2}}||_\Gamma^2 - ||\boldsymbol{J}_h^{n+\frac{1}{2}}||_\Gamma^2)\\
&+\frac{2\tau}{\sigma_0}||\overline{\boldsymbol{J}}_h^{n+1}||_\Gamma^2 = \tau\left[(H_h^{n+\frac{1}{2}}, \nabla\times\boldsymbol{E}_h^n) - (H_h^{n+\frac{3}{2}}, \nabla\times\boldsymbol{E}_h^{n+1})\right]\\
&+\tau\left[\langle\boldsymbol{E}_h^{n+1}, \boldsymbol{J}_h^{n+\frac{3}{2}}\rangle_\Gamma - \langle\boldsymbol{E}_h^n, \boldsymbol{J}_h^{n+\frac{1}{2}}\rangle_\Gamma\right] - 2\tau(K_s^{n+1}, \overline{H}_h^{n+1}).
\end{aligned} \tag{3.14}$$

Now summing up (3.14) over n from $n=0$ to any $m \le N_t-2$, and dropping the nonnegative term $\frac{2\tau}{\sigma_0}||\overline{\boldsymbol{J}}_h^{n+1}||_\Gamma^2$ on the left hand side of (3.14), we obtain

$$\epsilon_0(||\boldsymbol{E}_h^{m+1}||^2 - ||\boldsymbol{E}_h^0||^2) + \mu_0(||H_h^{m+\frac{3}{2}}||^2 - ||H_h^{\frac{1}{2}}||^2) + \frac{\tau_0}{\sigma_0}(||\boldsymbol{J}_h^{m+\frac{3}{2}}||_\Gamma^2 - ||\boldsymbol{J}_h^{\frac{1}{2}}||_\Gamma^2)$$

$$\leq \quad \tau\left[(H_h^{\frac{1}{2}}, \nabla\times \boldsymbol{E}_h^0) - (H_h^{m+\frac{3}{2}}, \nabla\times \boldsymbol{E}_h^{m+1})\right]$$
$$+\tau\left[\langle \boldsymbol{E}_h^{m+1}, \boldsymbol{J}_h^{m+\frac{3}{2}}\rangle_\Gamma - \langle \boldsymbol{E}_h^0, \boldsymbol{J}_h^{\frac{1}{2}}\rangle_\Gamma\right] - 2\tau\sum_{n=0}^{m}(K_s^{n+1}, \overline{H}_h^{n+1}). \tag{3.15}$$

By the inverse estimate (3.9), the Cauchy-Schwarz inequality, and the notation C_v, we have

$$\tau(H_h^{m+\frac{3}{2}}, \nabla\times \boldsymbol{E}_h^{m+1}) \leq \tau C_v\sqrt{\mu_0}||H_h^{m+\frac{3}{2}}||\cdot C_{in}h^{-1}\sqrt{\epsilon_0}||\boldsymbol{E}_h^{m+1}||$$
$$\leq \quad \frac{1}{2}\tau C_v C_{in}h^{-1}(\mu_0||H_h^{m+\frac{3}{2}}||^2 + \epsilon_0||\boldsymbol{E}_h^{m+1}||^2), \tag{3.16}$$

which also holds true for $m=-1$.

Similarly, by the trace estimate (3.10) and the Cauchy-Schwarz inequality, we have

$$\tau\langle \boldsymbol{E}_h^{m+1}, \boldsymbol{J}_h^{m+\frac{3}{2}}\rangle_\Gamma \leq \tau C_{tr}h^{-\frac{1}{2}}\sqrt{\frac{\sigma_0}{\epsilon_0\tau_0}}\cdot\sqrt{\epsilon_0}||\boldsymbol{E}_h^{m+1}||\cdot\sqrt{\frac{\tau_0}{\sigma_0}}||\boldsymbol{J}_h^{m+\frac{3}{2}}||_\Gamma$$
$$\leq \quad \frac{1}{2}\tau C_{tr}h^{-\frac{1}{2}}\sqrt{\frac{\sigma_0}{\epsilon_0\tau_0}}(\epsilon_0||\boldsymbol{E}_h^{m+1}||^2 + \frac{\tau_0}{\sigma_0}||\boldsymbol{J}_h^{m+\frac{3}{2}}||_\Gamma^2). \tag{3.17}$$

which also holds true for $m=-1$.

Finally, by the similar technique, we have

$$2\tau\sum_{n=0}^{m}(K_s^{n+1}, \overline{H}_h^{n+1}) \leq \tau\sum_{n=0}^{m}(\mu_0||\overline{H}_h^{n+1}||^2 + \frac{1}{\mu_0}||K_s^{n+1}||^2)$$
$$\leq \quad \tau\sum_{n=0}^{m}\left[\frac{\mu_0}{2}(||H_h^{n+\frac{3}{2}}||^2 + ||H_h^{n+\frac{1}{2}}||^2) + \frac{1}{\mu_0}||K_s^{n+1}||^2\right]$$
$$\leq \quad \frac{\tau\mu_0}{2}||H_h^{m+\frac{3}{2}}||^2 + \tau\sum_{n=0}^{m}\mu_0||H_h^{n+\frac{1}{2}}||^2 + \tau\sum_{n=0}^{m}\frac{1}{\mu_0}||K_s^{n+1}||^2. \tag{3.18}$$

Substituting the above estimates (3.16)-(3.18) into (3.15), and choosing τ small enough, such as

$$\tau \leq \frac{1}{2}, \quad \tau C_v C_{in}h^{-1} \leq \frac{1}{2}, \quad \tau C_{tr}h^{-\frac{1}{2}}\sqrt{\frac{\sigma_0}{\epsilon_0\tau_0}} \leq \frac{1}{2}, \tag{3.19}$$

which is equivalent to (3.12), we obtain

$$\frac{1}{2}\left(\epsilon_0||\boldsymbol{E}_h^{m+1}||^2 + \mu_0||H_h^{m+\frac{3}{2}}||^2 + \frac{\tau_0}{\sigma_0}||\boldsymbol{J}_h^{m+\frac{3}{2}}||_\Gamma^2\right)$$
$$\leq \quad \epsilon_0||\boldsymbol{E}_h^0||^2 + \mu_0||H_h^{\frac{1}{2}}||^2 + \frac{\tau_0}{\sigma_0}||\boldsymbol{J}_h^{\frac{1}{2}}||_\Gamma^2 + \tau\sum_{n=0}^{m}\frac{1}{\mu_0}||K_s^{n+1}||^2 + \tau\sum_{n=0}^{m}\mu_0||H_h^{n+\frac{1}{2}}||^2. \tag{3.20}$$

Using the discrete Gronwall inequality, we immediately have

$$\epsilon_0||\boldsymbol{E}_h^{m+1}||^2 + \mu_0||H_h^{m+\frac{3}{2}}||^2 + \frac{\tau_0}{\sigma_0}||\boldsymbol{J}_h^{m+\frac{3}{2}}||_\Gamma^2$$
$$\leq \quad 2\left[\epsilon_0||\boldsymbol{E}_h^0||^2 + \mu_0||H_h^{\frac{1}{2}}||^2 + \frac{\tau_0}{\sigma_0}||\boldsymbol{J}_h^{\frac{1}{2}}||_\Gamma^2 + \tau\sum_{n=0}^{m}\frac{1}{\mu_0}||K_s^{n+1}||^2\right]\cdot\exp(2(m+1)\tau), \tag{3.21}$$

which completes the proof of (3.13). □

By Theorem 3.1, it is easy to conclude the existence of a unique solution to our scheme.

Corollary 3.1. *Under the time constraint* (3.12)*, for all* $n \geq 0$*, there exists a unique solution* $\boldsymbol{E}_h^{n+1} \in \boldsymbol{V}_h^0$*,* $\boldsymbol{J}_h^{n+\frac{3}{2}} \times \hat{n} \in \boldsymbol{W}_h \times \hat{n}$*,* $H_h^{n+\frac{3}{2}} \in U_h$ *to the scheme* (3.1)-(3.3)*.*

3.2 Convergence analysis

To prove the error estimate for our scheme (3.1)-(3.3), we introduce the error notations:

$$\begin{aligned}\mathcal{E}_h^n &:= \boldsymbol{E}(t_n) - \boldsymbol{E}_h^n = (\boldsymbol{E}(t_n) - \Pi_c \boldsymbol{E}(t_n)) - (\boldsymbol{E}_h^n - \Pi_c \boldsymbol{E}(t_n)) := \boldsymbol{E}_{h\xi}^n - \boldsymbol{E}_{h\eta}^n, \quad (3.22)\\ \mathcal{H}_h^n &:= H(t_n) - H_h^n = (H(t_n) - \Pi_2 H(t_n)) - (H_h^n - \Pi_2 H(t_n)) := H_{h\xi}^n - H_{h\eta}^n, \quad (3.23)\end{aligned}$$

where $\boldsymbol{E}_{h\eta}^n, H_{h\eta}^n$ represent the errors between the finite element solutions and the interpolations or projections of the exact solutions, and $\boldsymbol{E}_{h\xi}^n, H_{h\xi}^n$ represent the interpolation or projection errors.

Moreover, we need the following lemma.

Lemma 3.1. [22, Lemmas 3.16 and 3.19] *Denote $u^n := u(\cdot, t_n)$. We have*

$$\begin{aligned}&(i) \quad \|\delta_\tau u^{n+\frac{1}{2}}\|^2 = \|\tfrac{u^{n+1}-u^n}{\tau}\|^2 \le \tfrac{1}{\tau}\int_{t_n}^{t_{n+1}} \|\partial_t u(t)\|^2\, dt, \quad \forall u \in H^1(0,T;L^2(\Omega)), \quad (3.24)\\ &(ii) \quad \|\overline{u}^{n+\frac{1}{2}} - \tfrac{1}{\tau}\int_{t_n}^{t_{n+1}} u(t)\, dt\|^2 \le \tfrac{\tau^3}{4}\int_{t_n}^{t_{n+1}} \|\partial_{tt} u(t)\|^2\, dt, \quad \forall u \in H^2(0,T;L^2(\Omega)), \quad (3.25)\\ &(iii) \quad \|u^{n+\frac{1}{2}} - \tfrac{1}{\tau}\int_{t_n}^{t_{n+1}} u(t)\, dt\|^2 \le \tfrac{\tau^3}{4}\int_{t_n}^{t_{n+1}} \|\partial_{tt} u(t)\|^2\, dt, \quad \forall u \in H^2(0,T;L^2(\Omega)). \quad (3.26)\end{aligned}$$

Integrating (2.9) with $\boldsymbol{\phi} = \boldsymbol{\phi}_h$ from $t = t_n$ to $t = t_{n+1}$, then dividing by τ, and using the result to subtract (3.1), we obtain the error equation for $\boldsymbol{E}$:

$$\begin{aligned}&\epsilon_0(\delta_\tau \boldsymbol{E}_h^{n+\frac{1}{2}}, \boldsymbol{\phi}_h) - (H_h^{n+\frac{1}{2}}, \nabla\times\boldsymbol{\phi}_h) + \langle \boldsymbol{J}^{n+\frac{1}{2}} - \boldsymbol{J}_h^{n+\frac{1}{2}}, \boldsymbol{\phi}_h\rangle_\Gamma,\\ =\ & (\frac{1}{\tau}\int_{t_n}^{t_{n+1}} H\ dt - H^{n+\frac{1}{2}}, \nabla\times\boldsymbol{\phi}_h) - \langle \frac{1}{\tau}\int_{t_n}^{t_{n+1}} \boldsymbol{J}\ dt - \boldsymbol{J}^{n+\frac{1}{2}}, \boldsymbol{\phi}_h\rangle_\Gamma, \quad (3.27)\end{aligned}$$

where for simplicity we denote the exact solutions $H^{n+\frac{1}{2}} := H(\cdot, t_{n+\frac{1}{2}})$ and $\boldsymbol{J}^{n+\frac{1}{2}} := \boldsymbol{J}(\cdot, t_{n+\frac{1}{2}})$.

Using the error notations (3.22)-(3.23), we can rewrite (3.27) as follows:

$$\begin{aligned}&\epsilon_0(\delta_\tau \boldsymbol{E}_{h\eta}^{n+\frac{1}{2}}, \boldsymbol{\phi}_h) - (H_{h\eta}^{n+\frac{1}{2}}, \nabla\times\boldsymbol{\phi}_h) + \langle \boldsymbol{J}_{h\eta}^{n+\frac{1}{2}}, \boldsymbol{\phi}_h\rangle_\Gamma\\ =\ & \epsilon_0(\delta_\tau \boldsymbol{E}_{h\xi}^{n+\frac{1}{2}}, \boldsymbol{\phi}_h) - (H_{h\xi}^{n+\frac{1}{2}}, \nabla\times\boldsymbol{\phi}_h) + \langle \boldsymbol{J}_{h\xi}^{n+\frac{1}{2}}, \boldsymbol{\phi}_h\rangle_\Gamma\\ &+(H^{n+\frac{1}{2}} - \frac{1}{\tau}\int_{t_n}^{t_{n+1}} H\ dt, \nabla\times\boldsymbol{\phi}_h) + \langle \frac{1}{\tau}\int_{t_n}^{t_{n+1}} \boldsymbol{J}\ dt - \boldsymbol{J}^{n+\frac{1}{2}}, \boldsymbol{\phi}_h\rangle_\Gamma, \quad (3.28)\end{aligned}$$

where we used the following simplified notations

$$\begin{aligned}\langle \boldsymbol{J}_{h\eta}^{n+\frac{1}{2}}, \boldsymbol{\phi}_h\rangle_\Gamma &= \int_\Gamma \Big(\boldsymbol{J}_h^{n+\frac{1}{2}} \times \hat{n} - \Pi_2(\boldsymbol{J}^{n+\frac{1}{2}} \times \hat{n})\Big)\cdot \boldsymbol{\phi}_h \times \hat{n}\ ds, \quad (3.29)\\ \langle \boldsymbol{J}_{h\xi}^{n+\frac{1}{2}}, \boldsymbol{\phi}_h\rangle_\Gamma &= \int_\Gamma \Big(\boldsymbol{J}^{n+\frac{1}{2}} \times \hat{n} - \Pi_2(\boldsymbol{J}^{n+\frac{1}{2}} \times \hat{n})\Big)\cdot \boldsymbol{\phi}_h \times \hat{n}\ ds. \quad (3.30)\end{aligned}$$

Similarly, integrating (2.10) with $\psi = \psi_h$ from $t = t_{n+\frac{1}{2}}$ to $t = t_{n+\frac{3}{2}}$, then dividing by τ, and using the result to subtract (3.2), we can obtain the error equation for H:

$$\begin{aligned}&\mu_0(\delta_\tau H_{h\eta}^{n+1}, \psi_h) + (\nabla\times\boldsymbol{E}_{h\eta}^{n+1}, \psi_h) = \mu_0(\delta_\tau H_{h\xi}^{n+1}, \psi_h) + (\nabla\times\boldsymbol{E}_{h\xi}^{n+1}, \psi_h)\\ &+(\frac{1}{\tau}\int_{t_{n+\frac{1}{2}}}^{t_{n+\frac{3}{2}}} \nabla\times\boldsymbol{E}\ dt - \nabla\times\boldsymbol{E}^{n+1}, \psi_h) + (\frac{1}{\tau}\int_{t_{n+\frac{1}{2}}}^{t_{n+\frac{3}{2}}} K_s\ dt - K_s^{n+1}, \psi_h). \quad (3.31)\end{aligned}$$

Finally, integrating (2.11) with $\psi = \psi_h$ from $t = t_{n+\frac{1}{2}}$ to $t = t_{n+\frac{3}{2}}$, then dividing by τ, and using the result to subtract (3.2), we can obtain the error equation for $\boldsymbol{J}$:

$$\begin{aligned}
&\tau_0\langle\delta_\tau \boldsymbol{J}_{h\eta}^{n+1}, \boldsymbol{\chi}_h\rangle_\Gamma + \langle\overline{\boldsymbol{J}}_{h\eta}^{n+1}, \boldsymbol{\chi}_h\rangle_\Gamma - \sigma_0\langle\boldsymbol{E}_{h\eta}^{n+1}, \boldsymbol{\chi}_h\rangle_\Gamma \\
= \;& \tau_0\langle\delta_\tau \boldsymbol{J}_{h\xi}^{n+1}, \boldsymbol{\chi}_h\rangle_\Gamma + \langle\overline{\boldsymbol{J}}_{h\xi}^{n+1}, \boldsymbol{\chi}_h\rangle_\Gamma - \sigma_0\langle\boldsymbol{E}_{h\xi}^{n+1}, \boldsymbol{\chi}_h\rangle_\Gamma \\
&+\langle\frac{1}{\tau}\int_{t_{n+\frac{1}{2}}}^{t_{n+\frac{3}{2}}} \boldsymbol{J}\ dt - \overline{\boldsymbol{J}}^{n+1}, \boldsymbol{\chi}_h\rangle_\Gamma - \sigma_0\langle(\frac{1}{\tau}\int_{t_{n+\frac{1}{2}}}^{t_{n+\frac{3}{2}}} \boldsymbol{E}\ dt - \boldsymbol{E}^{n+1}, \boldsymbol{\chi}_h\rangle_\Gamma. \qquad (3.32)
\end{aligned}$$

With the above error equations, we can prove the following error estimate for our scheme (3.1)-(3.3).

Theorem 3.2. *For the scheme* (3.1)-(3.3) *with initial approximations* (3.7)-(3.8)*, under the time step constraint* (3.12) *and the following regularity assumptions:*

$$\boldsymbol{E} \in L^\infty(0,T;H^r(curl;\Omega)),\ H \in L^\infty(0,T;H^r(\Omega)),\ \boldsymbol{J} \in L^\infty(0,T;L^2(\Gamma)), \qquad (3.33)$$

$$\partial_t \boldsymbol{E} \in L^2(0,T;H^r(curl;\Omega)),\ \partial_{tt}K_s, \partial_{tt}(\nabla\times\boldsymbol{E}) \in L^2(0,T;L^2(\Omega)), \qquad (3.34)$$

$$\partial_{tt}(\nabla\times H) \in L^2(0,T;(L^2(\Omega))^2),\ \partial_{tt}\boldsymbol{J},\ \partial_{tt}\boldsymbol{E} \in L^2(0,T;L^2(\Gamma)), \qquad (3.35)$$

we have: For any $0 \le m \le N_t - 1$,

$$\epsilon_0||\boldsymbol{E}_h^m - \boldsymbol{E}^m||^2 + \mu_0||H_h^{m+\frac{1}{2}} - H^{m+\frac{1}{2}}||^2 + \frac{\tau_0}{\sigma_0}||\boldsymbol{J}_h^{m+\frac{1}{2}} - \boldsymbol{J}^{m+\frac{1}{2}}||_\Gamma^2 \le C(\tau^3 + h^{2r-1}),$$

where the constant $C > 0$ *is independent of* τ *and* h*, and* $r \ge 1$ *is the order of the basis functions in spaces* U_h *and* $\boldsymbol{V}_h$*.*

Proof. Choosing $\boldsymbol{\phi}_h = 2\tau\overline{\boldsymbol{E}}_{h\eta}^{n+\frac{1}{2}}$, $\psi_h = 2\tau\overline{H}_{h\eta}^{n+1}$, $\boldsymbol{\chi}_h = \frac{2\tau}{\sigma_0}\overline{\boldsymbol{J}}_{h\eta}^{n+1}$ in (3.28)- (3.32), respectively, then adding them together, we have

$$\begin{aligned}
&\epsilon_0(||\boldsymbol{E}_{h\eta}^{n+1}||^2 - ||\boldsymbol{E}_{h\eta}^{n}||^2) + \mu_0(||H_{h\eta}^{n+\frac{3}{2}}||^2 - ||H_{h\eta}^{n+\frac{1}{2}}||^2) + \frac{\tau_0}{\sigma_0}(||\boldsymbol{J}_{h\eta}^{n+\frac{3}{2}}||_\Gamma^2 - ||\boldsymbol{J}_{h\eta}^{n+\frac{1}{2}}||_\Gamma^2) \\
&+\frac{2\tau}{\sigma_0}||\overline{\boldsymbol{J}}_{h\eta}^{n+1}||_\Gamma^2 = \tau\left[(H_{h\eta}^{n+\frac{1}{2}}, \nabla\times\boldsymbol{E}_{h\eta}^{n}) - (H_{h\eta}^{n+\frac{3}{2}}, \nabla\times\boldsymbol{E}_{h\eta}^{n+1})\right] \\
&\quad+\tau\left[\langle\boldsymbol{E}_{h\eta}^{n+1}, \boldsymbol{J}_{h\eta}^{n+\frac{3}{2}}\rangle_\Gamma - \langle\boldsymbol{E}_{h\eta}^{n}, \boldsymbol{J}_{h\eta}^{n+\frac{1}{2}}\rangle_\Gamma\right] \\
&\quad+2\tau\epsilon_0(\delta_\tau\boldsymbol{E}_{h\xi}^{n+\frac{1}{2}}, \overline{\boldsymbol{E}}_{h\eta}^{n+\frac{1}{2}}) - 2\tau(H_{h\xi}^{n+\frac{1}{2}}, \nabla\times\overline{\boldsymbol{E}}_{h\eta}^{n+\frac{1}{2}}) + 2\tau\langle\boldsymbol{J}_{h\xi}^{n+\frac{1}{2}}, \overline{\boldsymbol{E}}_{h\eta}^{n+\frac{1}{2}}\rangle_\Gamma \\
&+2\tau(H^{n+\frac{1}{2}} - \frac{1}{\tau}\int_{t_n}^{t_{n+1}} H\ dt, \nabla\times\overline{\boldsymbol{E}}_{h\eta}^{n+\frac{1}{2}}) + 2\tau\langle\frac{1}{\tau}\int_{t_n}^{t_{n+1}} \boldsymbol{J}\ dt - \boldsymbol{J}^{n+\frac{1}{2}}, \overline{\boldsymbol{E}}_{h\eta}^{n+\frac{1}{2}}\rangle_\Gamma \\
&+2\tau\mu_0(\delta_\tau H_{h\xi}^{n+1}, \overline{H}_{h\eta}^{n+1}) + 2\tau(\nabla\times\boldsymbol{E}_{h\xi}^{n+1}, \overline{H}_{h\eta}^{n+1}) \\
&+2\tau(\frac{1}{\tau}\int_{t_{n+\frac{1}{2}}}^{t_{n+\frac{3}{2}}} \nabla\times\boldsymbol{E}\ dt - \nabla\times\boldsymbol{E}^{n+1}, \overline{H}_{h\eta}^{n+1}) + 2\tau(\frac{1}{\tau}\int_{t_{n+\frac{1}{2}}}^{t_{n+\frac{3}{2}}} K_s\ dt - K_s^{n+1}, \overline{H}_{h\eta}^{n+1}) \\
&+\frac{2\tau\tau_0}{\sigma_0}\langle\delta_\tau\boldsymbol{J}_{h\xi}^{n+1}, \overline{\boldsymbol{J}}_{h\eta}^{n+1}\rangle_\Gamma + \frac{2\tau}{\sigma_0}\langle\overline{\boldsymbol{J}}_{h\xi}^{n+1}, \overline{\boldsymbol{J}}_{h\eta}^{n+1}\rangle_\Gamma - 2\tau\langle\boldsymbol{E}_{h\xi}^{n+1}, \overline{\boldsymbol{J}}_{h\eta}^{n+1}\rangle_\Gamma \\
&+\frac{2\tau}{\sigma_0}\langle\frac{1}{\tau}\int_{t_{n+\frac{1}{2}}}^{t_{n+\frac{3}{2}}} \boldsymbol{J}\ dt - \overline{\boldsymbol{J}}^{n+1}, \overline{\boldsymbol{J}}_{h\eta}^{n+1}\rangle_\Gamma - 2\tau\langle\frac{1}{\tau}\int_{t_{n+\frac{1}{2}}}^{t_{n+\frac{3}{2}}} \boldsymbol{E}\ dt - \boldsymbol{E}^{n+1}, \overline{\boldsymbol{J}}_{h\eta}^{n+1}\rangle_\Gamma. \qquad (3.36)
\end{aligned}$$

Summing up (3.36) from $n = 0$ to any $m \le N_t - 2$, we obtain

$$\epsilon_0(||\boldsymbol{E}_{h\eta}^{m+1}||^2 - ||\boldsymbol{E}_{h\eta}^{0}||^2) + \mu_0(||H_{h\eta}^{m+\frac{3}{2}}||^2 - ||H_{h\eta}^{\frac{1}{2}}||^2) + \frac{\tau_0}{\sigma_0}(||\boldsymbol{J}_{h\eta}^{m+\frac{3}{2}}||_\Gamma^2 - ||\boldsymbol{J}_{h\eta}^{\frac{1}{2}}||_\Gamma^2)$$

$$+\frac{2\tau}{\sigma_0}\sum_{n=0}^{m}||\overline{\boldsymbol{J}}_{h\eta}^{n+1}||_{\Gamma}^2 \leq \sum_{i=1}^{16} Err_i. \tag{3.37}$$

Now we just need to estimate each Err_i. Similar to the proofs of (3.16) and (3.17), we immediately have

$$\begin{aligned} & Err_1 = \tau\left[(H_{h\eta}^{\frac{1}{2}}, \nabla\times\boldsymbol{E}_{h\eta}^0) - (H_{h\eta}^{m+\frac{3}{2}}, \nabla\times\boldsymbol{E}_{h\eta}^{m+1})\right] \qquad (3.38)\\ \leq\ & \frac{1}{2}\tau C_v C_{in} h^{-1}(\mu_0||H_{h\eta}^{\frac{1}{2}}||^2 + \epsilon_0||\boldsymbol{E}_{h\eta}^0||^2) + \frac{1}{2}\tau C_v C_{in} h^{-1}(\mu_0||H_{h\eta}^{m+\frac{3}{2}}||^2 + \epsilon_0||\boldsymbol{E}_{h\eta}^{m+1}||^2), \end{aligned}$$

and

$$\begin{aligned} & Err_2 = \tau\left[\langle\boldsymbol{E}_{h\eta}^{m+1}, \boldsymbol{J}_{h\eta}^{m+\frac{3}{2}}\rangle_{\Gamma} - \langle\boldsymbol{E}_{h\eta}^0, \boldsymbol{J}_{h\eta}^{\frac{1}{2}}\rangle_{\Gamma}\right] \qquad (3.39)\\ \leq\ & \frac{1}{2}\tau C_{tr} h^{-\frac{1}{2}}\sqrt{\frac{\sigma_0}{\epsilon_0\tau_0}}(\epsilon_0||\boldsymbol{E}_{h\eta}^{m+1}||^2 + \frac{\tau_0}{\sigma_0}||\boldsymbol{J}_{h\eta}^{m+\frac{3}{2}}||_{\Gamma}^2) + \frac{1}{2}\tau C_{tr} h^{-\frac{1}{2}}\sqrt{\frac{\sigma_0}{\epsilon_0\tau_0}}(\epsilon_0||\boldsymbol{E}_{h\eta}^0||^2 + \frac{\tau_0}{\sigma_0}||\boldsymbol{J}_{h\eta}^{\frac{1}{2}}||_{\Gamma}^2). \end{aligned}$$

Using the inequality $(a,b) \leq \delta\|a\|^2 + \frac{1}{4\delta}\|b\|^2$, Lemma 3.1 (i), and the interpolation error estimate (3.4), we have

$$\begin{aligned} Err_3 &= \sum_{n=0}^{m} 2\tau\epsilon_0(\delta_\tau \boldsymbol{E}_{h\xi}^{n+\frac{1}{2}}, \overline{\boldsymbol{E}}_{h\eta}^{n+\frac{1}{2}}) \leq \sum_{n=0}^{m} 2\tau\epsilon_0\left(\delta_3||\overline{\boldsymbol{E}}_{h\eta}^{n+\frac{1}{2}}||^2 + \frac{1}{4\delta_3}||\delta_\tau \boldsymbol{E}_{h\xi}^{n+\frac{1}{2}}||^2\right)\\ &\leq \tau\epsilon_0\delta_3\sum_{n=0}^{m}(||\boldsymbol{E}_{h\eta}^{n+1}||^2 + ||\boldsymbol{E}_{h\eta}^{n}||^2) + \frac{\epsilon_0}{2\delta_3}\sum_{n=0}^{m}\int_{t_n}^{t_{n+1}} Ch^{2r}||\partial_t\boldsymbol{E}||_{H^r(curl;\Omega)}^2 dt. \qquad (3.40) \end{aligned}$$

Using the fact that $\nabla\times\overline{\boldsymbol{E}}_{h\eta}^{n+\frac{1}{2}} \in U_h$ and the projection operator property, we have

$$Err_4 = -2\tau\sum_{n=0}^{m}(H_{h\xi}^{n+\frac{1}{2}}, \nabla\times\overline{\boldsymbol{E}}_{h\eta}^{n+\frac{1}{2}}) = 0. \tag{3.41}$$

By the definition of (3.30), we have

$$Err_5 = 2\tau\sum_{n=0}^{m}\langle\boldsymbol{J}_{h\xi}^{n+\frac{1}{2}}, \overline{\boldsymbol{E}}_{h\eta}^{n+\frac{1}{2}}\rangle_{\Gamma} = 0. \tag{3.42}$$

Using integration by parts, the PEC boundary condition (2.7), the inequality $(a,b) \leq \delta\|a\|^2 + \frac{1}{4\delta}\|b\|^2$, and Lemma 3.1 (iii), we obtain

$$\begin{aligned} Err_6 &= 2\tau\sum_{n=0}^{m}(\nabla\times H^{n+\frac{1}{2}} - \frac{1}{\tau}\int_{t_n}^{t_{n+1}}\nabla\times H\ dt, \overline{\boldsymbol{E}}_{h\eta}^{n+\frac{1}{2}})\\ &\leq 2\tau C_v\sum_{n=0}^{m}\left(\delta_6\epsilon_0||\overline{\boldsymbol{E}}_{h\eta}^{n+\frac{1}{2}}||^2 + \frac{\mu_0}{4\delta_6}||\nabla\times H^{n+\frac{1}{2}} - \frac{1}{\tau}\int_{t_n}^{t_{n+1}}\nabla\times H\ dt||^2\right)\\ &\leq \tau C_v\delta_6\epsilon_0\sum_{n=0}^{m}(||\boldsymbol{E}_{h\eta}^{n+1}||^2 + ||\boldsymbol{E}_{h\eta}^{n}||^2) + \frac{\tau^4 C_v\mu_0}{8\delta_6}\sum_{n=0}^{m}\int_{t_n}^{t_{n+1}}||\partial_{tt}\nabla\times H||^2\ dt. \qquad (3.43) \end{aligned}$$

By the trace inequality and Lemma 3.1 (iii), we have

$$Err_7 = 2\tau\sum_{n=0}^{m}\langle\frac{1}{\tau}\int_{t_n}^{t_{n+1}}\boldsymbol{J}\ dt - \boldsymbol{J}^{n+\frac{1}{2}}, \overline{\boldsymbol{E}}_{h\eta}^{n+\frac{1}{2}}\rangle_{\Gamma}$$

$$
\begin{aligned}
&\leq 2\tau\sum_{n=0}^{m}||\frac{1}{\tau}\int_{t_n}^{t_{n+1}}\boldsymbol{J}\ dt-\boldsymbol{J}^{n+\frac{1}{2}}||_{\Gamma}\cdot C_{tr}h^{-\frac{1}{2}}||\overline{\boldsymbol{E}}_{h\eta}^{n+\frac{1}{2}}||\\
&\leq 2\tau\sum_{n=0}^{m}\left(\delta_7\epsilon_0||\overline{\boldsymbol{E}}_{h\eta}^{n+\frac{1}{2}}||^2+\frac{C_{tr}^2h^{-1}}{4\delta_7\epsilon_0}\cdot\frac{\tau^3}{4}\int_{t_n}^{t_{n+1}}||\partial_{tt}\boldsymbol{J}||_{\Gamma}^2\ dt\right)\\
&\leq \tau\delta_7\epsilon_0\sum_{n=0}^{m}(||\boldsymbol{E}_{h\eta}^{n+1}||^2+||\boldsymbol{E}_{h\eta}^{n}||^2)+\frac{C_{tr}^2\tau^4h^{-1}}{8\delta_7\epsilon_0}\sum_{n=0}^{m}\int_{t_n}^{t_{n+1}}||\partial_{tt}\boldsymbol{J}||_{\Gamma}^2\ dt. \qquad (3.44)
\end{aligned}
$$

By the L^2 projection property, we have

$$
Err_8=2\tau\mu_0\sum_{n=0}^{m}(\delta_\tau H_{h\xi}^{n+1},\overline{H}_{h\eta}^{n+1})=0. \qquad (3.45)
$$

Using the interpolation error estimate (3.4), we have

$$
\begin{aligned}
&Err_9=2\tau\sum_{n=0}^{m}(\nabla\times\boldsymbol{E}_{h\xi}^{n+1},\overline{H}_{h\eta}^{n+1})\leq 2\tau C_v\sum_{n=0}^{m}\left(\delta_9\mu_0||\overline{H}_{h\eta}^{n+1}||^2+\frac{\epsilon_0}{4\delta_9}||\nabla\times\boldsymbol{E}_{h\xi}^{n+1}||^2\right)\\
\leq\ &\tau C_v\delta_9\mu_0\sum_{n=0}^{m}(||H_{h\eta}^{n+\frac{3}{2}}||^2+||H_{h\eta}^{n+\frac{1}{2}}||^2)+\frac{\tau C_v\epsilon_0}{\delta_9}\sum_{n=0}^{m}Ch^{2r}||\boldsymbol{E}||^2_{L^\infty(0,T;H^r(curl;\Omega))}. \qquad (3.46)
\end{aligned}
$$

By Lemma 3.1 (iii), we have

$$
\begin{aligned}
Err_{10} &= 2\tau\sum_{n=0}^{m}(\frac{1}{\tau}\int_{t_{n+\frac{1}{2}}}^{t_{n+\frac{3}{2}}}\nabla\times\boldsymbol{E}\ dt-\nabla\times\boldsymbol{E}^{n+1},\overline{H}_{h\eta}^{n+1})\\
&\leq 2\tau C_v\sum_{n=0}^{m}\left(\delta_{10}\mu_0||\overline{H}_{h\eta}^{n+1}||^2+\frac{\epsilon_0}{4\delta_{10}}||\frac{1}{\tau}\int_{t_{n+\frac{1}{2}}}^{t_{n+\frac{3}{2}}}\nabla\times\boldsymbol{E}\ dt-\nabla\times\boldsymbol{E}^{n+1}||^2\right) \qquad (3.47)\\
&\leq \tau C_v\delta_{10}\mu_0\sum_{n=0}^{m}(||H_{h\eta}^{n+\frac{3}{2}}||^2+||H_{h\eta}^{n+\frac{1}{2}}||^2)+\frac{\tau^4C_v\epsilon_0}{8\delta_{10}}\sum_{n=0}^{m}\int_{t_{n+\frac{1}{2}}}^{t_{n+\frac{3}{2}}}||\partial_{tt}\nabla\times\boldsymbol{E}||^2\ dt.
\end{aligned}
$$

Similar to Err_{10}, we have

$$
\begin{aligned}
Err_{11} &= 2\tau\sum_{n=0}^{m}(\frac{1}{\tau}\int_{t_{n+\frac{1}{2}}}^{t_{n+\frac{3}{2}}}K_s\ dt-K_s^{n+1},\overline{H}_{h\eta}^{n+1}) \qquad (3.48)\\
&\leq \tau C_v\delta_{11}\mu_0\sum_{n=0}^{m}(||H_{h\eta}^{n+\frac{3}{2}}||^2+||H_{h\eta}^{n+\frac{1}{2}}||^2)+\frac{\tau^4C_v\epsilon_0}{8\delta_{11}}\sum_{n=0}^{m}\int_{t_{n+\frac{1}{2}}}^{t_{n+\frac{3}{2}}}||\partial_{tt}K_s||^2\ dt.
\end{aligned}
$$

By the definition of (3.30), we obtain

$$
Err_{12}=\frac{2\tau\tau_0}{\sigma_0}\sum_{n=0}^{m}\langle\delta_\tau\boldsymbol{J}_{h\xi}^{n+1},\overline{\boldsymbol{J}}_{h\eta}^{n+1}\rangle_\Gamma=0, \qquad (3.49)
$$

and

$$
Err_{13}=\frac{2\tau}{\sigma_0}\sum_{n=0}^{m}\langle\overline{\boldsymbol{J}}_{h\xi}^{n+1},\overline{\boldsymbol{J}}_{h\eta}^{n+1}\rangle_\Gamma=0. \qquad (3.50)
$$

By the trace inequality and the interpolation error estimate (3.4), we have

$$Err_{14} = -2\tau \sum_{n=0}^{m} \langle \boldsymbol{E}_{h\xi}^{n+1}, \overline{\boldsymbol{J}}_{h\eta}^{n+1} \rangle_{\Gamma} \leq 2\tau \sum_{n=0}^{m} C_{tr} h^{-\frac{1}{2}} ||\boldsymbol{E}_{h\xi}^{n+1}|| \cdot ||\overline{\boldsymbol{J}}_{h\eta}^{n+1}||_{\Gamma}$$

$$\leq \quad \tau\delta_{14} \sum_{n=0}^{m} (||\boldsymbol{J}_{h\eta}^{n+\frac{3}{2}}||_{\Gamma}^2 + ||\boldsymbol{J}_{h\eta}^{n+\frac{1}{2}}||_{\Gamma}^2) + \frac{\tau C_{tr}^2 h^{2r-1}}{2\delta_{14}} \sum_{n=0}^{m} ||\boldsymbol{E}||_{L^{\infty}(0,T;H^r(curl;\Omega))}^2. \quad (3.51)$$

By Lemma 3.1 (ii), we have

$$Err_{15} \quad = \quad \frac{2\tau}{\sigma_0} \sum_{n=0}^{m} \langle \frac{1}{\tau} \int_{t_{n+\frac{1}{2}}}^{t_{n+\frac{3}{2}}} \boldsymbol{J} \, dt - \overline{\boldsymbol{J}}^{n+1}, \overline{\boldsymbol{J}}_{h\eta}^{n+1} \rangle_{\Gamma}$$

$$\leq \quad \frac{\tau\delta_{15}}{\sigma_0} \sum_{n=0}^{m} (||\boldsymbol{J}_{h\eta}^{n+\frac{3}{2}}||_{\Gamma}^2 + ||\boldsymbol{J}_{h\eta}^{n+\frac{1}{2}}||_{\Gamma}^2) + \frac{\tau^4}{8\delta_{15}\sigma_0} \sum_{n=0}^{m} \int_{t_{n+\frac{1}{2}}}^{t_{n+\frac{3}{2}}} ||\partial_{tt}\boldsymbol{J}||_{\Gamma}^2 \, dt. \quad (3.52)$$

Similarly, by Lemma 3.1 (iii), we have

$$Err_{16} \quad = \quad -2\tau \sum_{n=0}^{m} \langle \frac{1}{\tau} \int_{t_{n+\frac{1}{2}}}^{t_{n+\frac{3}{2}}} \boldsymbol{E} \, dt - \boldsymbol{E}^{n+1}, \overline{\boldsymbol{J}}_{h\eta}^{n+1} \rangle_{\Gamma}$$

$$\leq \quad \tau\delta_{16} \sum_{n=0}^{m} (||\boldsymbol{J}_{h\eta}^{n+\frac{3}{2}}||_{\Gamma}^2 + ||\boldsymbol{J}_{h\eta}^{n+\frac{1}{2}}||_{\Gamma}^2) + \frac{\tau^4}{8\delta_{16}} \sum_{n=0}^{m} \int_{t_{n+\frac{1}{2}}}^{t_{n+\frac{3}{2}}} ||\partial_{tt}\boldsymbol{E}||_{\Gamma}^2 \, dt. \quad (3.53)$$

Substituting the above estimates of Err_i into (3.37), combining like terms together, and dropping the last nonnegative term on the left hand side, we obtain

$$\begin{aligned}
&\epsilon_0(||\boldsymbol{E}_{h\eta}^{m+1}||^2 - ||\boldsymbol{E}_{h\eta}^{0}||^2) + \mu_0(||H_{h\eta}^{m+\frac{3}{2}}||^2 - ||H_{h\eta}^{\frac{1}{2}}||^2) + \frac{\tau_0}{\sigma_0}(||\boldsymbol{J}_{h\eta}^{m+\frac{3}{2}}||_{\Gamma}^2 - ||\boldsymbol{J}_{h\eta}^{\frac{1}{2}}||_{\Gamma}^2) \\
\leq \quad & \frac{1}{2}\tau C_v C_{in} h^{-1}(\mu_0||H_{h\eta}^{\frac{1}{2}}||^2 + \epsilon_0||\boldsymbol{E}_{h\eta}^{0}||^2) + \frac{1}{2}\tau C_{tr} h^{-\frac{1}{2}} \sqrt{\frac{\sigma_0}{\epsilon_0\tau_0}}(\epsilon_0||\boldsymbol{E}_{h\eta}^{0}||^2 + \frac{\tau_0}{\sigma_0}||\boldsymbol{J}_{h\eta}^{\frac{1}{2}}||_{\Gamma}^2) \\
&+ \left(\frac{1}{2}\tau C_v C_{in} h^{-1} + \tau C_v\delta_9 + \tau C_v\delta_{10} + \tau C_v\delta_{11}\right)\mu_0||H_{h\eta}^{m+\frac{3}{2}}||^2 \\
&+ \left(\frac{1}{2}\tau C_v C_{in} h^{-1} + \frac{1}{2}\tau C_{tr} h^{-\frac{1}{2}}\sqrt{\frac{\sigma_0}{\epsilon_0\tau_0}} + \tau\delta_3 + \tau C_v\delta_6 + \tau\delta_7\right)\epsilon_0||\boldsymbol{E}_{h\eta}^{m+1}||^2 \\
&+ \left(\frac{1}{2}\tau C_{tr} h^{-\frac{1}{2}}\sqrt{\frac{\sigma_0}{\epsilon_0\tau_0}} + \frac{\tau\delta_{14}\sigma_0}{\tau_0} + \frac{\tau\delta_{15}}{\tau_0} + \frac{\tau\delta_{16}\sigma_0}{\tau_0}\right)\frac{\tau_0}{\sigma_0}||\boldsymbol{J}_{h\eta}^{m+\frac{3}{2}}||_{\Gamma}^2 \\
&+ \tau(2\delta_3 + 2C_v\delta_6 + 2\delta_7)\epsilon_0 \sum_{n=0}^{m} ||\boldsymbol{E}_{h\eta}^{n}||^2 + \tau(2C_v\delta_9 + 2C_v\delta_{10} + 2C_v\delta_{11})\mu_0 \sum_{n=0}^{m} ||H_{h\eta}^{n+\frac{1}{2}}||^2 \\
&+ \tau(\frac{2\sigma_0\delta_{14}}{\tau_0} + \frac{2\delta_{15}}{\tau_0} + \frac{2\sigma_0\delta_{16}}{\tau_0})\frac{\tau_0}{\sigma_0}\sum_{n=0}^{m} ||\boldsymbol{J}_{h\eta}^{n+\frac{1}{2}}||_{\Gamma}^2 \qquad (3.54) \\
&+ \frac{\epsilon_0 C h^{2r}}{2\delta_3}\int_0^T ||\partial_t\boldsymbol{E}||_{H^r(curl;\Omega)}^2 dt + (\frac{TC_v\epsilon_0 C h^{2r}}{\delta_9} + \frac{TC_{tr}^2 h^{2r-1}}{2\delta_{14}})||\boldsymbol{E}||_{L^{\infty}(0,T;H^r(curl;\Omega))}^2 \\
&+ \frac{\tau^4 C_v\mu_0}{8\delta_6}\int_0^T ||\partial_{tt}\nabla\times H||^2 \, dt + (\frac{C_{tr}^2\tau^4 h^{-1}}{8\delta_7\epsilon_0} + + \frac{\tau^4}{8\delta_{15}\sigma_0})\int_0^T ||\partial_{tt}\boldsymbol{J}||_{\Gamma}^2 \, dt \\
&+ \frac{\tau^4 C_v\epsilon_0}{8\delta_{10}}\int_0^T ||\partial_{tt}\nabla\times\boldsymbol{E}||^2 \, dt + \frac{\tau^4 C_v\epsilon_0}{8\delta_{11}}\int_0^T ||\partial_{tt}K_s||^2 \, dt + \frac{\tau^4}{8\delta_{16}}\int_0^T ||\partial_{tt}\boldsymbol{E}||_{\Gamma}^2 \, dt.
\end{aligned}$$

Under the same time step constraint (3.12), by using the discrete Gronwall inequality and choosing those δ_i properly, such as

$$\delta_9 = \delta_{10} = \delta_{11} = \frac{1}{8C_v},\ \delta_3 = \delta_7 = \frac{1}{16},\ \delta_6 = \frac{1}{8C_v},\ \delta_{14} = \delta_{16} = \frac{\tau_0}{8\sigma_0},\ \delta_{15} = \frac{\tau_0}{8},$$

we have

$$\begin{aligned} & \epsilon_0 ||\boldsymbol{E}_{h\eta}^{m+1}||^2 + \mu_0 ||H_{h\eta}^{m+\frac{3}{2}}||^2 + \frac{\tau_0}{\sigma_0} ||\boldsymbol{J}_{h\eta}^{m+\frac{3}{2}}||_\Gamma^2 \qquad (3.55) \\ \leq\ & C\left(\epsilon_0 ||\boldsymbol{E}_{h\eta}^0||^2 + \mu_0 ||H_{h\eta}^{\frac{1}{2}}||^2 + \frac{\tau_0}{\sigma_0} ||\boldsymbol{J}_{h\eta}^{\frac{1}{2}}||_\Gamma^2 + h^{2r-1} + \tau^3\right) \exp(12(m+1)\tau) \leq C(h^{2r-1} + \tau^3), \end{aligned}$$

where in the last step we used the following initial approximation error estimates

$$||\boldsymbol{E}_h^0 - \boldsymbol{E}^0|| \leq Ch^r,\ ||H_h^{\frac{1}{2}} - H^{\frac{1}{2}}|| \leq C(h^r + \tau^2),\ ||\boldsymbol{J}_h^{\frac{1}{2}} - \boldsymbol{J}^{\frac{1}{2}}||_\Gamma \leq C(h^r + \tau^2). \qquad (3.56)$$

Finally, using the triangle inequality, the interpolation error estimate (3.4), and the L^2 projection error estimate, from (3.55) we conclude the proof. □

4 Numerical results

In this section, we present several numerical examples to demonstrate the effectiveness of our graphene model in simulating the propagation of surface plasmon polaritons (SPPs) on graphene sheets. Our numerical tests are carried out by using FEniCS [25].

4.1 Test of convergence rates

The first example is developed to test the theoretical convergence rate of our numerical scheme by a manufactured exact solution:

$$\begin{aligned} \mathbf{E}(x,y,t) &= \begin{pmatrix} E_x \\ E_y \end{pmatrix} = \begin{pmatrix} \sin(2\pi x)\sin(2\pi y) sin(2\pi t) \\ \cos(2\pi x)\cos(2\pi y) sin(2\pi t) \end{pmatrix}, \\ \mathbf{J}(x,y,t) &= \begin{pmatrix} J_x \\ J_y \end{pmatrix} = \begin{pmatrix} \frac{1}{1+4\pi^2}\sin(2\pi x)\sin(2\pi y)(\sin(2\pi t) - 2\pi\cos(2\pi t) + 2\pi\exp(-t)) \\ \frac{1}{1+4\pi^2}\cos(2\pi x)\cos(2\pi y)(\sin(2\pi t) - 2\pi\cos(2\pi t) + 2\pi\exp(-t)) \end{pmatrix}, \\ H_1(x,y,t) &= \frac{1}{1+4\pi^2}\sin(2\pi x)\sin(2\pi y)\sin(2\pi t), \\ H_2(x,y,t) &= \frac{1}{1+4\pi^2}\sin(2\pi x)\sin(2\pi y)(2\pi\cos(2\pi t) - 2\pi\exp(-t)), \end{aligned}$$

which satisfies the following graphene model equations:

$$\epsilon_0 \partial_t \boldsymbol{E} = \nabla \times H_1 - \boldsymbol{J} + \boldsymbol{f}_1, \quad \text{in } \Omega_1, \qquad (4.1)$$

$$\mu_0 \partial_t H_1 = -\nabla \times \boldsymbol{E} + f_2, \quad \text{in } \Omega_1, \qquad (4.2)$$

$$\tau_0 \partial_t \boldsymbol{J} + \boldsymbol{J} = \sigma_0 \boldsymbol{E}, \quad \text{on } \Gamma, \qquad (4.3)$$

$$\epsilon_0 \partial_t \boldsymbol{E} = \nabla \times H_2 - \boldsymbol{J} + \boldsymbol{f}_3, \quad \text{in } \Omega_2, \qquad (4.4)$$

$$\mu_0 \partial_t H_2 = -\nabla \times \boldsymbol{E} + f_4, \quad \text{in } \Omega_2. \tag{4.5}$$

Here the added source terms $\boldsymbol{f}_1, f_2, \boldsymbol{f}_3$ and f_4 can be calculated from the given exact solution $\boldsymbol{E}, H_1, H_2$ and $\boldsymbol{J}$.

For simplicity, we choose the physical domain $\Omega = (0,1)^2$, which is split into two subdomains $\Omega_1 = (0,1) \times (0.5,1)$ and $\Omega_2 = (0,1) \times (0,0.5)$ with interface $\Gamma = \{y = 0.5, x \in [0,1]\}$. We apply our developed scheme (3.1)-(3.3) to solve (4.1)-(4.5) with physical parameters $\epsilon_0 = \mu_0 = \tau_0 = \sigma_0 = 1$.

First, we solve this example with a fixed small time step size $\tau = 1 \times 10^{-4}$ and various mesh sizes for $N_t = 1000$ time steps. The obtained L^2 errors are presented in Tables 1 and 2 for the RTN finite element spaces U_h and $\boldsymbol{V}_h$ with $r = 1, 2$, respectively. Our results show that the obtained L^2 errors are at least $O(h^{r-0.5})$ for $r = 1, 2$, respectively.

Table 1: The errors obtained for Example 1 with $N_t = 1000, \tau = 1 \times 10^{-4}, r = 1$.

h	$\|\boldsymbol{E} - \boldsymbol{E}_h\|_{L^2(\Omega)}$	rate	$\|H - H_h\|_{L^2(\Omega)}$	rate	$\|\boldsymbol{J} - \boldsymbol{J}_h\|_{\Gamma}$	rate
1/4	1.9581×10^{-2}		5.0621×10^{-4}		9.8589×10^{-5}	
1/8	9.9814×10^{-3}	0.9721	2.4718×10^{-4}	1.0341	5.0621×10^{-4}	0.9721
1/16	5.0220×10^{-3}	0.9909	1.1794×10^{-4}	1.0674	5.0255×10^{-5}	0.9909
1/32	2.5152×10^{-3}	0.9975	5.4204×10^{-5}	1.1216	2.5285×10^{-5}	0.9975
1/64	1.2581×10^{-3}	0.9993	2.3716×10^{-5}	1.1925	1.2663×10^{-5}	0.9993
1/128	6.3045×10^{-4}	0.9968	1.2374×10^{-5}	0.9385	3.1693×10^{-6}	0.9990

Table 2: The errors obtained for Example 1 with $N_t = 1000, \tau = 1 \times 10^{-4}, r = 2$.

h	$\|\boldsymbol{E} - \boldsymbol{E}_h\|_{L^2(\Omega)}$	rate	$\|H - H_h\|_{L^2(\Omega)}$	rate	$\|\boldsymbol{J} - \boldsymbol{J}_h\|_{\Gamma}$	rate
1/4	4.4129×10^{-3}		2.5281×10^{-4}		2.2218×10^{-5}	
1/8	1.0730×10^{-3}	2.0400	1.2988×10^{-4}	0.9607	5.4012×10^{-6}	2.0403
1/16	2.6160×10^{-4}	2.0361	6.3906×10^{-5}	1.0232	1.3113×10^{-6}	2.0422
1/32	6.8419×10^{-5}	1.9349	2.1809×10^{-5}	1.5510	3.2979×10^{-7}	1.9913
1/64	2.1824×10^{-5}	1.6484	4.0333×10^{-6}	2.4349	9.2774×10^{-8}	1.8297
1/128	6.9954×10^{-6}	1.6414	1.0048×10^{-6}	2.0050	2.9704×10^{-8}	1.6430

Then we test the convergence rate in terms of τ by fixing $\tau = \frac{h}{200}$ to guarantee the stability constraint. The obtained L^2 errors are presented in Tables 3-4 for $r = 1, 2$, respectively, and they are at least $O(\tau^{1.5})$. When $r = 1$, due to the time step constraint $\tau = O(h)$, the theoretical convergence rate should be dominated by $O(h^{0.5}) = O(\tau^{0.5})$, but our numerical errors are better and almost $O(h)$.

Table 3: The obtained errors obtained for $r = 1$ by fixing $\tau = \frac{h}{200}$.

h	$\|\boldsymbol{E} - \boldsymbol{E}_h\|_{L^2(\Omega)}$	rate	$\|H - H_h\|_{L^2(\Omega)}$	rate	$\|\boldsymbol{J} - \boldsymbol{J}_h\|_{\Gamma}$	rate
1/10	8.0084×10^{-3}		2.0027×10^{-4}		4.1938×10^{-5}	
1/20	4.0208×10^{-3}	0.9940	9.3324×10^{-5}	1.1016	2.0546×10^{-5}	0.9721
1/40	2.0126×10^{-3}	0.9984	4.1560×10^{-5}	1.1670	1.0158×10^{-5}	0.9909
1/80	1.0066×10^{-3}	0.9995	1.8654×10^{-5}	1.1556	5.0491×10^{-6}	0.9975
1/160	5.0537×10^{-4}	0.9940	1.0326×10^{-5}	0.8532	2.5194×10^{-6}	0.9993

Table 4: The obtained errors obtained for $r = 2$ by fixing $\tau = \frac{h}{200}$.

h	$\|\boldsymbol{E} - \boldsymbol{E}_h\|_{L^2(\Omega)}$	rate	$\|H - H_h\|_{L^2(\Omega)}$	rate	$\|\boldsymbol{J} - \boldsymbol{J}_h\|_{\Gamma}$	rate
1/10	6.7883×10^{-4}		1.0984×10^{-4}		3.5527×10^{-6}	
1/20	1.6779×10^{-4}	2.0164	4.8473×10^{-5}	1.1801	8.4889×10^{-7}	2.0652
1/40	4.5943×10^{-5}	1.8687	1.3049×10^{-5}	1.8931	2.1569×10^{-6}	1.9765
1/80	1.7540×10^{-5}	1.3892	3.5181×10^{-6}	1.8911	6.5890×10^{-7}	1.7108
1/160	6.9715×10^{-6}	1.3311	9.6548×10^{-7}	1.8654	2.1517×10^{-8}	1.6145

4.2 Simulation of surface plasmon polaritons along the graphene sheets

To simulate the SPP phenomenon on the graphene sheet, we need to use a PML to surround the physical domain Ω. Here we adopt the 2D TEz Ziolkowski PML model in the PML region Ω_{pml}, which can be written as follows (cf. [32, p.157]):

$$\epsilon_0\partial_t\boldsymbol{E} = -\epsilon_0 D_1\boldsymbol{E} + \nabla\times H_z - \boldsymbol{J}, \quad \text{in } \Omega_{pml}, \tag{4.6}$$

$$\mu_0\partial_t H = -\mu_0(\sigma_x+\sigma_y)H_z - \nabla\times\boldsymbol{E} - K_z, \quad \text{in } \Omega_{pml}, \tag{4.7}$$

$$\partial_t\boldsymbol{J} = -D_2\boldsymbol{J} + \epsilon_0 D_3\boldsymbol{E}, \quad \text{in } \Omega_{pml}, \tag{4.8}$$

$$\partial_t K_z = \mu_0\sigma_x\sigma_y H_z, \quad \text{in } \Omega_{pml}, \tag{4.9}$$

where $\sigma_x(x)$ and $\sigma_y(y)$ are the nonnegative damping functions in the x and y directions, respectively, the diagonal matrices D_i $(i=1,2,3)$ are given as follows:

$$D_1 = diag(\sigma_y-\sigma_x, \sigma_x-\sigma_y),\ D_2 = diag(\sigma_x,\sigma_y),\ D_3 = diag(\sigma_x(\sigma_x-\sigma_y), \sigma_y(\sigma_y-\sigma_x)). \tag{4.10}$$

We propose the following finite element scheme for the above PML model in Ω_{pml}: For any $n\geq 0$, find $\boldsymbol{E}_h^{n+1}, \boldsymbol{J}_h^{n+\frac{3}{2}} \in \boldsymbol{V}_h^0$, $H_h^{n+\frac{3}{2}}, K_{zh}^{n+1} \in U_h$ such that

$$\epsilon_0(\delta_\tau\boldsymbol{E}_h^{n+\frac{1}{2}}, \boldsymbol{\phi}_h) = -\epsilon_0(D_1\overline{\boldsymbol{E}}_h^{n+\frac{1}{2}}, \boldsymbol{\phi}_h) + (H_{zh}^{n+\frac{1}{2}}, \nabla\times\boldsymbol{\phi}_h) - (\boldsymbol{J}_h^{n+\frac{1}{2}}, \boldsymbol{\phi}_h), \tag{4.11}$$

$$\mu_0(\delta_\tau H_{zh}^{n+1}, \psi_h) = -\mu_0((\sigma_x+\sigma_y)\overline{H}_{zh}^{n+1}, \psi_h) - (\nabla\times\boldsymbol{E}_h^{n+1}, \psi_h) - (K_{zh}^{n+1}, \psi_h), \tag{4.12}$$

$$(\delta_\tau\boldsymbol{J}_h^{n+1}, \boldsymbol{\chi}_h) = -(D_2\overline{\boldsymbol{J}}_h^{n+1}, \boldsymbol{\chi}_h) + \epsilon_0(D_3\boldsymbol{E}_h^{n+1}, \boldsymbol{\chi}_h), \tag{4.13}$$

$$(\delta_\tau K_{zh}^{n+\frac{1}{2}}, \varphi_h) = \mu_0(\sigma_x\sigma_y H_{zh}^{n+\frac{1}{2}}, \varphi_h), \tag{4.14}$$

hold true for any test functions $\boldsymbol{\phi}_h \in \boldsymbol{V}_h^0, \psi_h, \varphi_h \in U_h$ and $\boldsymbol{\chi}_h \in W_h$.

To simplify the implementation, we merge the graphene scheme (3.1)-(3.3) and the PML scheme (4.11)-(4.14) together by using subdomain dependent coefficients and rewrite them as follows:

$$\begin{aligned}\left(\epsilon_0(I+\frac{\tau D_1}{2})\boldsymbol{E}_h^{n+1}, \boldsymbol{\phi}_h\right) &= \left(\epsilon_0(I-\frac{\tau D_1}{2})\boldsymbol{E}_h^{n}, \boldsymbol{\phi}_h\right) + \tau(H_h^{n+\frac{1}{2}}, \nabla\times\boldsymbol{\phi}_h)\\ &\quad + \tau\langle\boldsymbol{J}_h^{n+\frac{1}{2}}, \boldsymbol{\phi}_h\rangle_\Gamma - \tau(C_{id}\boldsymbol{J}_h^{n+\frac{1}{2}}, \boldsymbol{\phi}_h),\end{aligned} \tag{4.15}$$

$$\begin{aligned}\left(\mu_0(1+\frac{\tau(\sigma_x+\sigma_y)}{2})H_h^{n+\frac{3}{2}}, \psi_h\right) &= \left(\mu_0(1-\frac{\tau(\sigma_x+\sigma_y)}{2})H_h^{n+\frac{1}{2}}, \psi_h\right) - \tau(\nabla\times\boldsymbol{E}_h^{n+1}, \psi_h)\\ &\quad - \tau(C_{id}K_h^{n+1}, \psi_h) - \tau(K_{sh}^{n+1}, \psi_h),\end{aligned} \tag{4.16}$$

$$\begin{aligned}\left((I+\frac{\tau D_2}{2})\boldsymbol{J}_h^{n+\frac{3}{2}}, \boldsymbol{\chi}_h\right) + \langle(1+\frac{\tau}{2\tau_0})\boldsymbol{J}_h^{n+\frac{3}{2}}, \boldsymbol{\chi}_h\rangle_\Gamma &= \left((I-\frac{\tau D_2}{2})J_h^{n+\frac{1}{2}}, \boldsymbol{\chi}_h\right) + \tau(\epsilon_0 D_3\boldsymbol{E}_h^{n+1}, \boldsymbol{v}_h)\\ &\quad + \langle(1-\frac{\tau}{2\tau_0})J_h^{n+\frac{1}{2}}, \boldsymbol{\chi}_h\rangle_\Gamma + \tau\langle\frac{\sigma_0}{\tau_0}\boldsymbol{E}_h^{n+1}, \boldsymbol{\chi}_h\rangle_\Gamma,\end{aligned} \tag{4.17}$$

$$(K_h^{n+1}, \varphi_h) = (K_h^n, \varphi_h) + \tau\mu_0(\sigma_x\sigma_y H_h^{n+\frac{1}{2}}, \varphi_h), \tag{4.18}$$

where we denote the identity matrix $I = diag(1,1)$, write H_{zh} and J_{zh} in the PML subdomain as H_h and J_h, and use the subdomain identify function

$$C_{id} = \begin{cases} 0, & \text{if } \boldsymbol{x}\in\Omega, \\ 1, & \text{if } \boldsymbol{x}\in\Omega_{pml}. \end{cases} \tag{4.19}$$

In our simulation, we choose a physical domain $\overline{\Omega} = [-30, 30]\ \mu m \times [-10, 10]\ \mu m$, which is surrounded by the Ziolkowski PML with thickness $12h_x$ and $12h_y$ in the x and y directions, respectively, where h_x and h_y are the mesh sizes in the x and y directions, respectively. We use a uniformly refined triangular mesh with 128×128 rectangles bisected into triangles.

The damping functions σ_x and σ_y for the PML are chosen as a fourth order polynomial:

$$\sigma_x(x) = \begin{cases} \sigma_{max}(\frac{|x|-30}{dd})^4, & \text{when } |x| \geq 30, \\ 0, & elsewhere, \end{cases}$$

where the coefficient $\sigma_{max} = -\log(err) \cdot 5 \cdot C_v/(2 \cdot dd)$ with $err = 10^{-7}$, and dd denotes the thickness of the PML in the x direction. The function σ_y has the same form but varies with respect to the y variables.

Example 1: A straight graphene sheet

In this example, we present a simulation of SPPs along one graphene sheet aligned horizontally. The simulation setup is shown in Fig. 1, where a graphene sheet of $40\mu m$ long is embedded in domain Ω. Outside of Ω is surrounded by the PML.

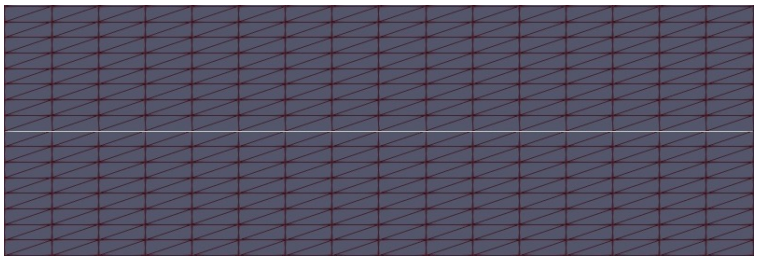

Figure 1: The setup demonstration (with a coarse mesh) for Example 1.

A pair of dipole source waves are placed at points $(-27, 1)\ \mu m$ and $(-27, -1)\ \mu m$, and imposed as $K_s = \sin(2\pi f_0 t)/h_y$ and $K_s = -\sin(2\pi f_0 t)/h_y, respectively.$ In our simulation, we choose frequency $f_0 = 10\ THz$, relaxation time $\tau_0 = 1.2\ ps$, and the surface conductivity σ_0 given by the formula:

$$\sigma_0 = -\frac{q^2 k_B T \tau_0}{\pi \hbar^2} \left(\frac{\mu_c}{k_B T} + 2\ln(\exp(-\frac{\mu_c}{k_B T}) + 1) \right), \tag{4.20}$$

where the electron charge $q = 1.6022e - 19$, the Kelvin temperature $T = 300\ K$, the reduced Plank constant $\hbar = 1.0546e - 34$, the Boltzman constant $k_B = 1.3806e - 23$, and the chemical potential $\mu_c = 1.5\ eV$.

We use the time step $\tau = 8.3 \times 10^{-17}\ s$, and run the simulation for 10000 time steps. Some snapshots of the obtained magnetic filed H_z are shown in Fig. 2, which clearly show the SPPs propagate along the graphene sheet.

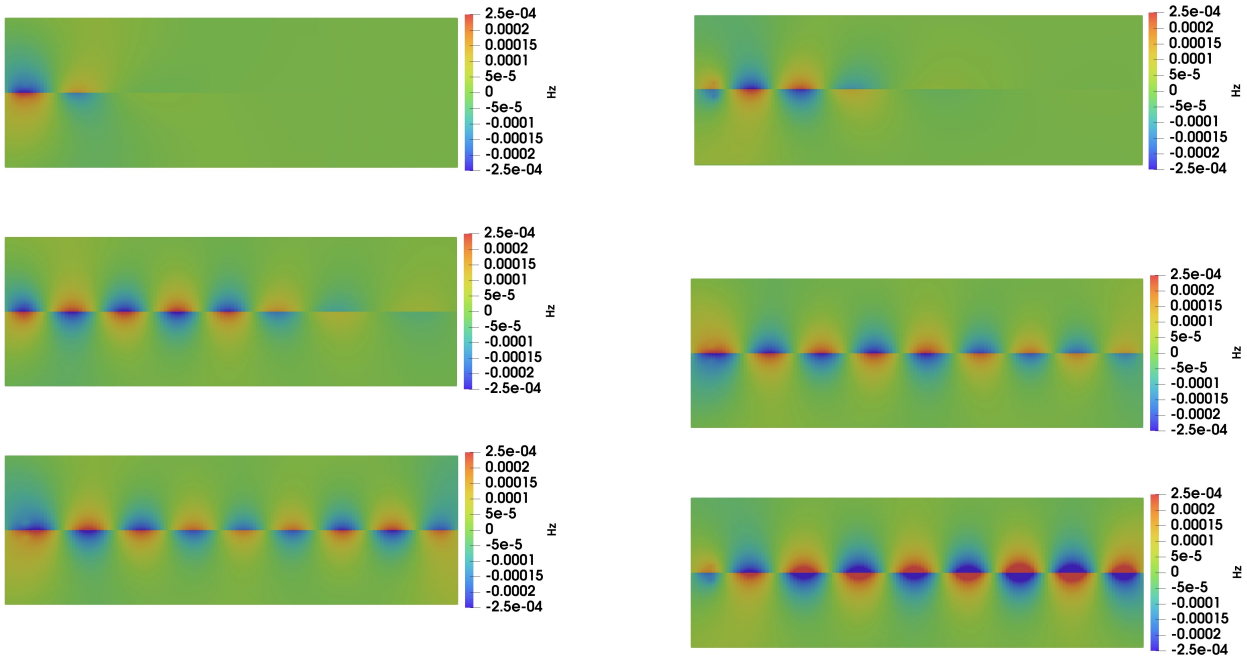

Figure 2: Example 1. Contour plots of H_z at 1000, 2000, 4000, 6000, 8000, and 10000 time steps.

Example 2: Four adjacent graphene sheets

In this example, we simulate the wave propagation along four adjacent graphene sheets by our FETD scheme. The simulation setup is shown in Fig. 3, where four graphene sheets of length 10 μm each is embedded in domain Ω_0. A pair of dipole incident waves are placed at points $(-27, 3.12)$ μm) and $(-27, -3.12)$ μm. We use the same simulation parameters as Example 1. Some snapshots of the magnetic field H_z are presented in Fig. 4, which shows clearly that the SPPs propagate along the graphene sheets as demonstrated in the previous work [39].

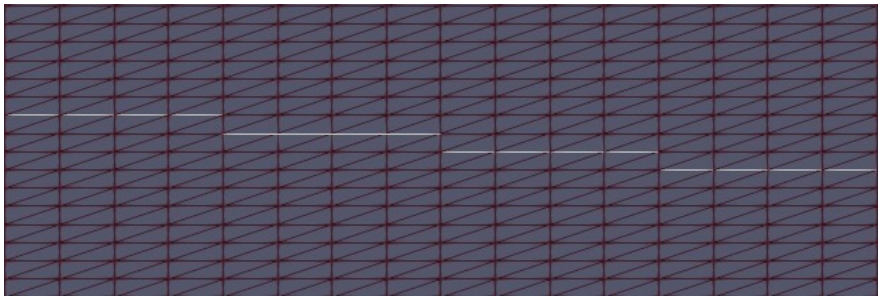

Figure 3: Example 2. The setup (shown in a coarse mesh) for four adjacent graphene sheets buried in Ω.

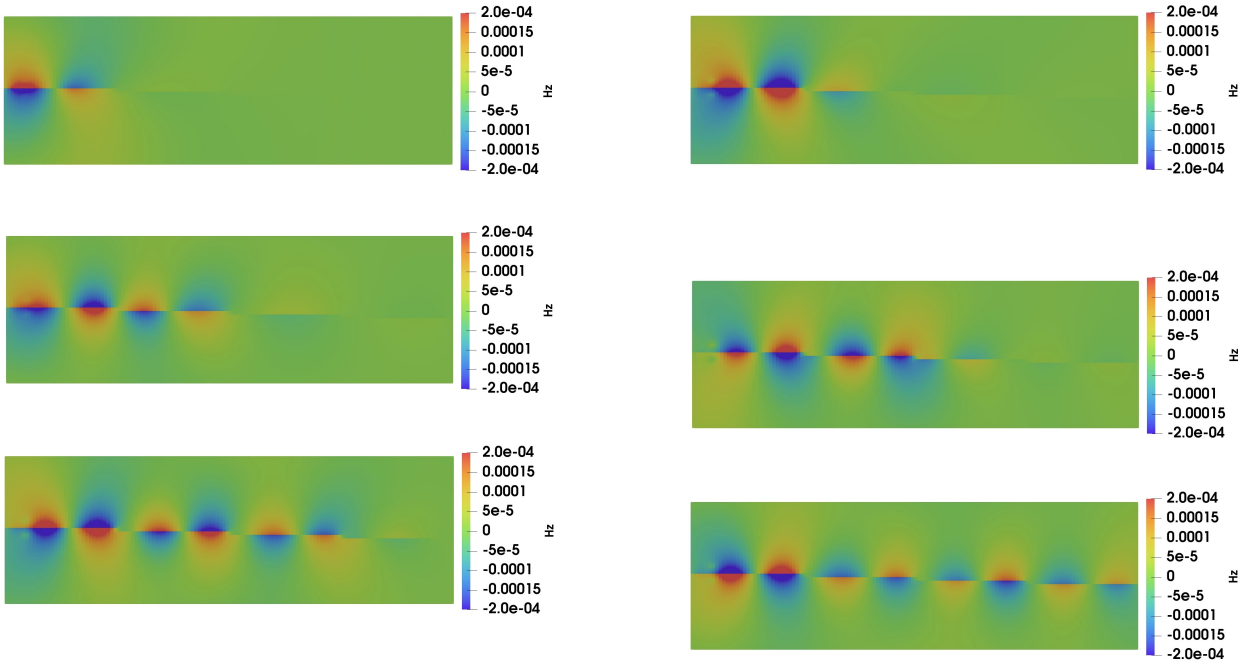

Figure 4: Example 2. Contour plots of H_z obtained at 1000, 2000, 4000, 6000, 8000, and 10000 time steps.

Example 3: A tilted graphene sheet

This example is developed to simulate the propagation of SPPs along a tilted graphene sheet by our FETD scheme. The simulation setup is shown in Fig. 5, where one tilted graphene sheet situating on the line $y = \frac{1}{3}x$ with length $20\sqrt{5}$ μm is embedded in domain Ω_0. A pair of dipole source waves are placed at points $(-21, -6)$ μm and $(-21, -8)$ μm. The rest of the simulation data are the same as Example 1. The calculated magnetic fields H_z obtained at different time steps are presented in Fig. 6, which shows that the SPPs also propagate along this tilted graphene sheet.

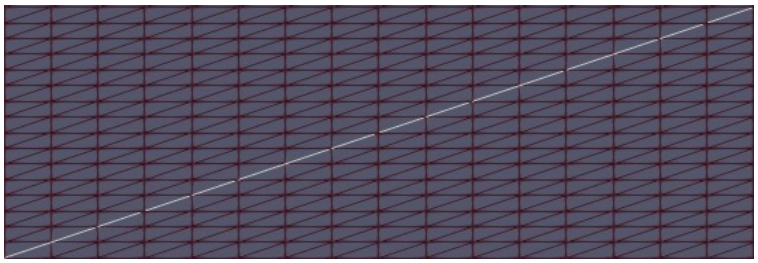

Figure 5: Example 3. The setup for the tilted graphene sheet.

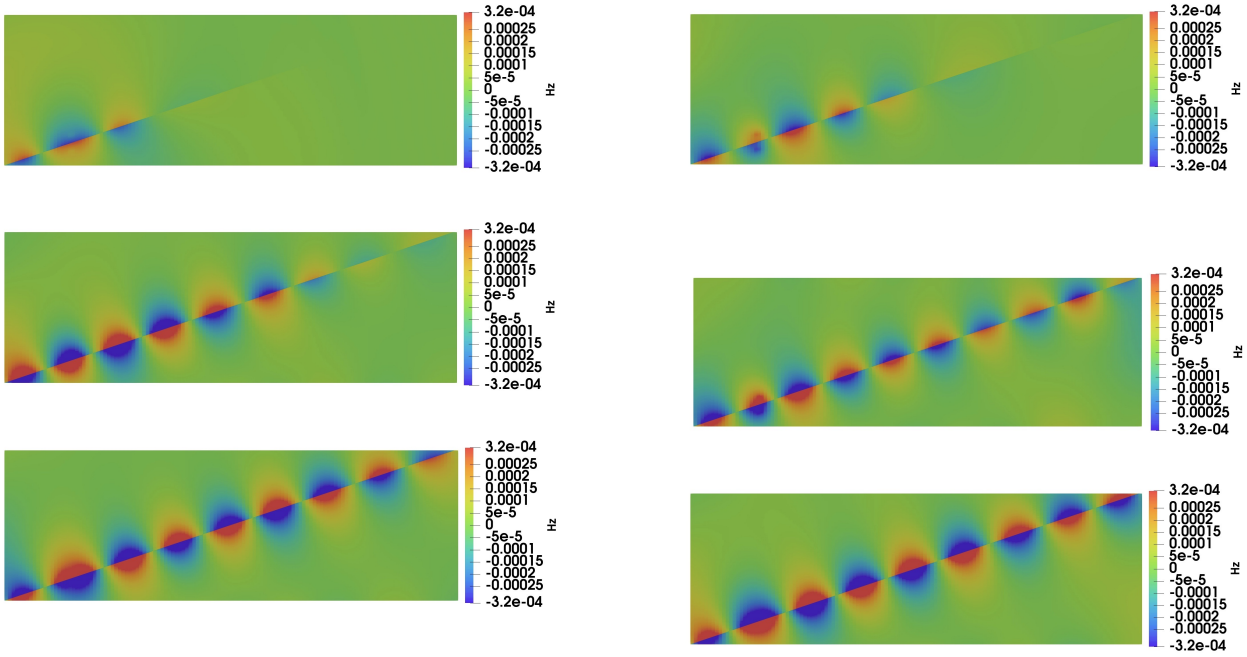

Figure 6: Example 3. Contour plots of H_z obtained at 1000, 2000, 4000, 6000, 8000, and 10000 time steps.

Example 4: SPPs propagating along along a bifurcated graphene sheet

Finally, we present a bifurcated graphene sheet to demonstrate the flexibility of our FETD scheme to handle a complicated geometry. The simulation setup is illustrated in Fig. 7, and the rest simulation data are kept the same as Example 1. The obtained numerical magnetic fields H_z at various time steps are presented in Fig. 8, which shows that the SPPs can propagate along this complicated graphene sheet.

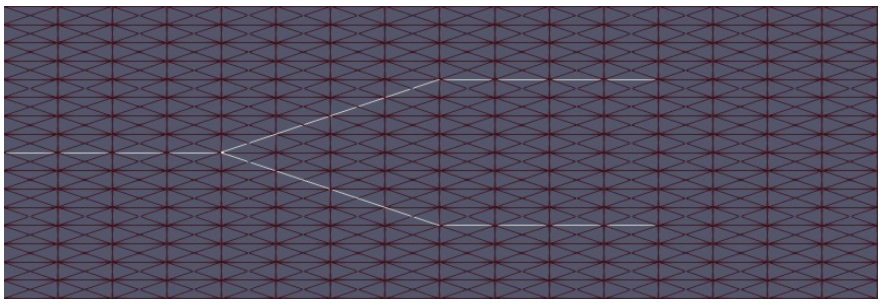

Figure 7: Example 4. The simulation setup for the bifurcated graphene sheet (illustrated with a coarse mesh).

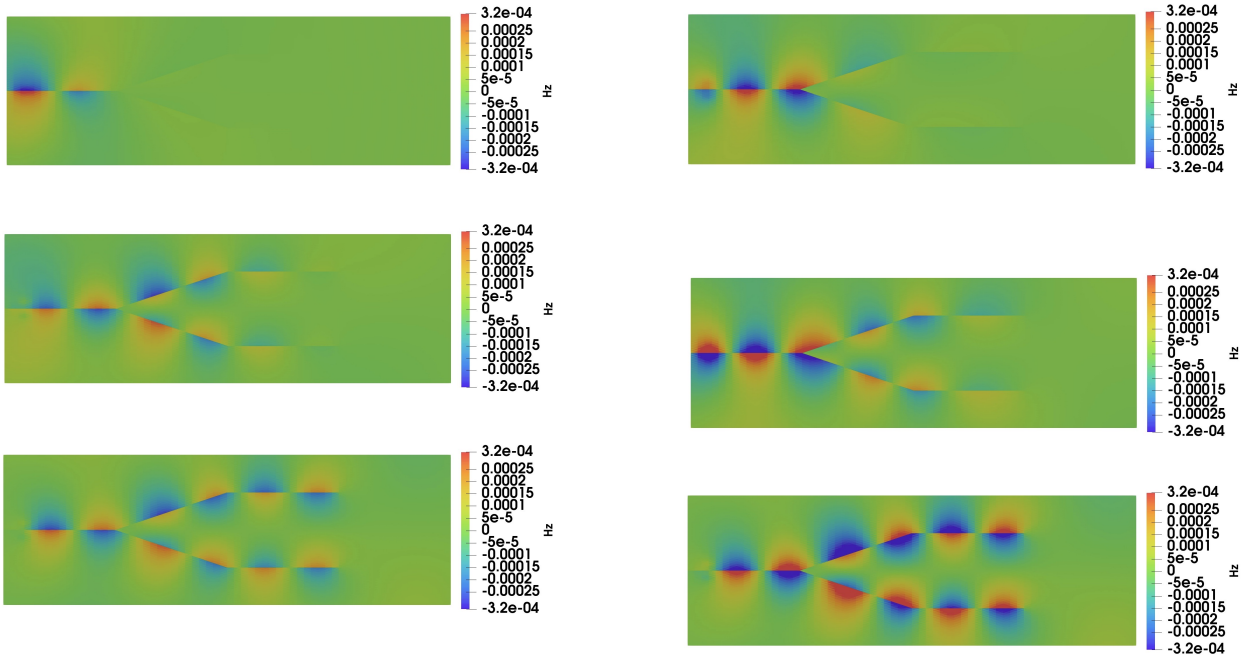

Figure 8: Example 4. Contour plots of H_z at 500, 1000, 2000, 4000, 6000, and 10000 time steps.

5 Conclusion

In this paper, we develop a new formulation to simulate the surface plasmon polaritons propagating on graphene sheets. We treat the graphene as a thin sheet of current with an effective conductivity. A novel finite element method is proposed for solving this graphene model. Numerical results demonstrate the effectiveness of this graphene model for simulating the surface plasmon polaritons propagating on graphene sheets. The current error estimate is sub-optimal and the loss of half-order accuracy is caused by those graphene interface terms $Err_i, i = 2, 7, 14$. We will continue exploring more efficient and optimally convergent schemes in the future, since much works are needed for the time-dependent $H(curl; \Omega)$-interface problem as pointed out in the last sentence of Conclusion in [13].

Acknowledgements. The authors are very grateful to two anonymous referees for their insightful comments on improving the paper.

6 Declarations

Funding Li's work is supported by NSF grant DMS-2011943.

Conflicts of Interests/Competing Interest The authors have no conflicts of interest to declare that are relevant to the content of this article.

References

[1] X. Bai, S. Wang and H. Rui, Numerical analysis of finite-difference time-domain method for 2D/3D Maxwell's equations in a Cole-Cole dispersive medium, Comput. Math. Appl. 93 (2021) 230-252.

[2] Y.V. Bludov, A. Ferreira, N. Peres, M.I. Vasileskiy, A primer on surface plasmon-polaritons in graphene, Int. J. Modern Phys. 27 (10) (2013) 1341001

[3] D. Boffi, M. Costabel, M. Dauge, L. Demkowicz and R. Hiptmair, Discrete compactness for the p-version of discrete differential forms, SIAM J. Numer. Anal. 49 (2011) 135-158.

[4] F. Bonaccorso, Z. Sun, T. Hasan and A.C. Ferrari, Graphene photonics and optoelectronics, Nature Photonics 4 (2010) 611-622.

[5] G.D. Bouzianas, N.V. Kantartzis, C.S. Antonopoulos and T.D. Tsiboukis, Optimal modeling of infinite graphene sheets via a class of generalized FDTD schemes, IEEE Transactions on Magnetics 48(2) (2012) 379-382.

[6] A. Buffa, P. Houston and I. Perugia, Discontinuous Galerkin computation of the Maxwell eigenvalues on simplicial meshes, J. Comput. Appl. Math. 204 (2007) 317-333.

[7] C. Carstensen, L. Demkowicz and J. Gopalakrishnan, Breaking spaces and forms for the DPG method and applications including Maxwell equations, Comput. Math. Appl. 72(3) (2016) 494-522.

[8] Z. Chen, Q. Du and J. Zou, Finite element methods with matching and nonmatching meshes for Maxwell equations with discontinuous coefficients, SIAM J. Numer. Anal. 37 (2000) 1542-1570.

[9] L. Demkowicz, J. Kurtz, D. Pardo, M. Paszynski, W. Rachowicz and A. Zdunek, Computing with hp-Adaptive Finite Elements. vol. 2: Frontiers: Three Dimensional Elliptic and Maxwell Problems with Applications, CRC Press, Taylor and Francis, 2008.

[10] E. Fan, J. Wang, Y. Liu, H. Li and Z. Fang, Numerical simulations based on shifted second-order difference/finite element algorithms for the time fractional Maxwell's system, Eng. Comput. 38 (2022) 191-205.

[11] A. Fisher, J. Alvarez and N.L. Gibson, Analysis of methods for the Maxwell-random Lorentz model, Results Appl. Math. 8 (2020) 100098.

[12] A.K. Geim and K.S. Novoselov, The rise of graphene, Nature Materials 6(3) (2007) 183-191.

[13] R. Hiptmair, J. Li and J. Zou, Convergence analysis of finite element methods for H(curl;Ω)-elliptic interface problems, Numer. Math. 122(3) (2012) 557-578.

[14] J. Hong, L. Ji and L. Kong, Energy-dissipation splitting finite-difference time-domain method for Maxwell equations with perfectly matched layers, J. Comput. Phys. 269 (2014) 201-214.

[15] Y. Huang, M. Chen, J. Li and Y. Lin, Numerical analysis of a leapfrog ADI–FDTD method for Maxwell's equations in lossy media, Comput. Math. Appl. 76 (2018) 938-956.

[16] Y. Huang, J. Li and Q. Lin, Superconvergence analysis for time-dependent Maxwell's equations in metamaterials, Numer. Methods Partial Differential Eq. 28 (2012) 1794-1816.

[17] Y. Huang, J. Li and W. Yang, Modeling backward wave propagation in metamaterials by the finite element time domain method, SIAM J. Sci. Comput. 35 (2013) B248-B274.

[18] Y. Huang, J. Li and W. Yang, Developing and analyzing a finite element method for simulating wave propagation in graphene-based absorber, Comput. Math. Appl. 122 (2022) 76-92.

[19] M.J. Jenkinson and J.W. Banks, High-order accurate FDTD schemes for dispersive Maxwell's equations in second-order form using recursive convolutions, J. Comput. Appl. Math. 336 (2018) 192-218.
[20] J. Li, Two new finite element schemes and their analysis for modeling of wave propagation in graphene, Results Appl. Math. 9 (2021) Article 100136, 21pp.
[21] J. Li and J. Hesthaven, Analysis and application of the nodal discontinuous Galerkin method for wave propagation in metamaterials, J. Comput. Phys. 258 (2014) 915-930.
[22] J. Li and Y. Huang, Time-Domain Finite Element Methods for Maxwell's Equations in Metamaterials, Springer Ser. Comput. Math. 43, Springer, New York, 2013.
[23] P. Li, L. J. Jiang and H. Bagci, Discontinuous Galerkin time-domain modeling of graphene nano-ribbon incorporating the spatial dispersion effects, IEEE Trans. Antennas Propag. 66(7) (2018) 3590-3598.
[24] W. Li, D. Liang and Y. Lin, A new energy-conserved S-FDTD scheme for Maxwell's equations in metamaterials, Int. J. Numer. Anal. Model. 10 (2013) 775-794.
[25] A. Logg, K.-A. Mardal and G.N. Wells (eds.), Automated Solution of Differential Equations by the Finite Element Method: The FEniCS Book, Springer, 2012.
[26] M. Maier, D. Margetis and M. Luskin, Dipole excitation of surface plasmon on a conducting sheet: finite element approximation and validation, J. Comput. Phys. 339 (2017) 126-145.
[27] A. Mock, Padé approximant spectral fit for FDTD simulation of graphene in the near infrared, Optical Materials Express 2(6) (2012) 771-781.
[28] P. Monk, Finite Element Methods for Maxwell's Equations, Oxford University Press, Oxford, 2003.
[29] V. Nayyeri, M. Soleimani and O.M. Ramahi, Wideband modeling of graphene using the finite-difference time-domain method, IEEE Trans. Antennas Propag. 61(12) (2013) 6107-6114.
[30] K.S. Novoselov, A.K. Geim, S.V. Morozov, D. Jiang, Y. Zhang, S.V. Dubonos, I.V. Grigorieva and A.A. Firsov, Electric field effect in atomically thin carbon films, Science 306 (2004) 666-669.
[31] C. Scheid and S. Lanteri, Convergence of a Discontinuous Galerkin scheme for the mixed time domain Maxwell's equations in dispersive media, IMA J. Numer. Anal. 33(2) (2013) 432-459.
[32] C. Shi, J. Li and C.-W. Shu, Discontinuous Galerkin methods for Maxwell's equations in Drude metamaterials on unstructured meshes, J. Comput. Appl. Math. 342 (2018) 147-163.
[33] J.H. Song, M. Maier and M. Luskin, Adaptive finite element simulations of waveguide configurations involving parallel 2D material sheets, Comput. Methods Appl. Mech. Engrg. 351 (2019) 20-34.
[34] A. Taflove and S.C. Hagness, Computational Electrodynamics: The Finite-Difference Time-Domain Method, 3rd ed., Norwood, MA: Artech, 2005.
[35] A. Vakil and N. Engheta, Transformation optics using graphene, Science, Vol.332, Issue 6035 (2011) 1291-1294.
[36] B. Wang, Z. Yang, L.-L. Wang and S. Jiang, On time-domain NRBC for Maxwell's equations and its application in accurate simulation of electromagnetic invisibility cloaks, J. Sci. Comput. 86(2) (2021) Paper 20.
[37] P. Wang, Y. Shi, C.-Y. Tian and L. Li, Analysis of graphene-based devices using wave equation based discontinuous Galerkin time-domain method, IEEE Antennas Wireless Propag. Lett. 17(12) (2018) 2169-2173.

[38] J. Wilson, F. Santosa and P. A. Martin, Temporally manipulated plasmons on graphene, SIAM J. Appl. Math. 79(3) (2019) 1051-1074.
[39] W. Yang, J. Li and Y. Huang, Time-domain finite element method and analysis for modeling of surface plasmon polaritons, Comput. Methods Appl. Mech. Engrg. 372 (2020) 113349.
[40] Y. Zhang, D.D. Nguyen, K. Du, J. Xu and S. Zhao, Time-domain numerical solutions of Maxwell interface problems with discontinuous electromagnetic waves, Adv. Appl. Math. Mech. 8 (2016) 353-385.